Computational fluid dynamics challenge on indoor dispersion of pathogen-laden aerosols

Jordi Pallares[1], Alexandre Fabregat[1]*, Akim Lavrinenko[1], Nelson Marques[2,3], Bruno Santos[2], Gabriele Mosca[4], Pedro Obando Vega[4], Jure Ravnik[5], Nejc Vovk[5], Bruño Fraga[6], Aleksandra Monka[6], Manuel Martínez[7], Naomi Mestre-Curto[7], Francisco Jose de Souza[8], Douglas Fontes[9], Natalie Jüngling[10], Jennifer Niessner[10], Robert Castilla[11], Mercè Garcia Vílchez[11], David F. Fletcher[12], Kiao Inthavong[13], Matjaž Hriberšek[5], Paul Steinmann[14], Jana Wedel[14], Florent Duchaine[15], Shriram Sankurantripati[15], Leo Amari[16], Gábor Janiga[16], Cristian Marchioli[17], Salvatore Cito[1]

[1]Departament d'Enginyeria Mecànica, Universitat Rovira i Virgili, Av. Països Catalans, 26, 43007-Tarragona, Spain.

[2] FS Dynamics Portugal, Rua Fonte dos Corvos 29, Casais da Serra, 2665-305 Milharado, Portugal.

[3]Department of Mechanical Engineering, ISEL, Rua Conselheiro Emídio Navarro 35, 1950-062 Lisboa, Portugal.

[4]Buildwind, Rue Bara 175, 1070 Brussels, Belgium.

[5]Faculty of Mechanical Engineering, University of Maribor, Smetanova 17, SI-2000, Maribor, Slovenia.

[6]Department of Civil Engineering, University of Birmingham, Edgbaston, Birmingham, B15 2TT, United Kingdom.

[7]Eurecat, Centre Tecnològic de Catalunya, Water, Air and Soil Unit, C. Marcel·lí Domingo 2, 43007-Tarragona, Spain.

[8]School of Mechanical Engineering, Federal University of Uberlândia, Uberlândia 38400-902, Brazil.

[9]Engineering Program, Westmont College, 955 La Paz Rd, Santa Barbara, CA 93108, United States of America.

[10]Institute for Flow in Additively Manufactured Porous Media, Heilbronn University of Applied Sciences, Max-Planck-Str. 39, 74081-Heilbronn, Germany.

[11]CATMech- Fluid Mechanics Department, Universitat Politècnica de Catalunya, Carrer Colom, 1-11, 08222-Terrassa, Spain.

[12]School of Chemical and Biomolecular Engineering, The University of Sydney, Sydney, Australia.

[13]Mechanical & Automotive Engineering, School of Engineering, RMIT University, Bundoora, Victoria 3083, Australia.

[14]Institute of Applied Mechanics, University of Erlangen Nuremberg, Erlangen, Germany.

[15]CERFACS, 42 Avenue Gaspard Coriolis, 31 057 Toulouse, Cedex 01, France.

[16]Laboratory of Fluid Dynamics and Technical Flows, Otto von Guericke University of Magdeburg, Germany.

[17]Department of Engineering and Architecture, University of Udine, Via delle Scienze 208, 33100 Udine, Italy.

*Corresponding author: alexandre.fabregat@urv.cat

ABSTRACT

This paper presents and discusses the results of the "2024 International Computational Fluid Dynamics Challenge on the long-range indoor dispersion of pathogen-laden aerosols" aimed at assessing the ability of different computational codes and turbulence models to reproduce the dispersion of particles produced by a turbulent natural convection flow enclosed in a room sized cubical cavity. A total of twelve research groups from ten different countries have conducted fifteen simulations of the same flow configuration by solving the Reynolds Averaged Navier-Stokes (RANS) equations, the Unsteady Reynolds Averaged Navier-Stokes (URANS) equations or using Scale Adaptive Simulations (SAS), Large-Eddy Simulations (LES) or hybrid (URANS-LES) techniques. Results of the velocity field and of the particle dispersion provided by the different simulations are compared extensively, also including the reference results provided by a Direct Numerical Simulation (DNS). In general, LES and hybrid methods reproduce the time averaged flow field correctly, the spatial distribution of the turbulence kinetic energy and the particle dispersion. The performance of SAS is similar to that of LES and hybrid methods while the predictions of the RANS and URANS simulations exhibit larger deviations with respect to DNS. In general, the particle dispersion is better reproduced by simulations that capture correctly the spatial distribution of the turbulence kinetic energy.

Keywords: Aerosol dispersion, Natural convection, Turbulence, Cubical cavity, CFD challenge

1. INTRODUCTION

Good indoor air quality is important for human health. Long-term exposure to air pollution can cause several health problems (Maroni et al., 1995). The list of potential contaminants is long and includes chemicals, smoke, biological pollutants and particulate matter (PM), among others (Jones, 1999; Seguel et al., 2017; WHO, 2010). Indoor PM encompasses solid and/or liquid particles suspended in air and concerns are focused on particles that are 10 micrometers in size or smaller (PM10) because these particles are inhalable and can affect the lungs and the heart (Riley et al. 2002; Tan and Zhang, 2003). Indoor PM is generated, among other sources, by cooking, cleaning and combustion activities, printers, animals, mold as well as humans, when breathing, speaking, singing, sneezing or coughing (Li et al., 2017). The pathogen-laden aerosols generated during these respiratory events by an infected person are known to be the route of transmission of some respiratory diseases (Bourouiba, 2021).

Computational Fluid Dynamics (CFD) has been essential in analyzing and predicting indoor airflows in the last decades (Li and Nielsen, 2011). Most of the CFD based studies have been oriented towards understanding and improving ventilation strategies (Cuce et al. 2019, Yerragolam et al., 2020), determining the exposure to pollutants (Shen et al. 2013, Choi et al., 2019; Concilio et al., 2024), analysis of the dispersion and deposition of PM (Xu and Wang, 2017) or establishing the risk of infection by pathogen laden aerosols (Ai and Melikov, 2018, Sheiknejad et al., 2022; Shim et al., 2023). Simulations of indoor ventilation have been performed mostly using the numerical solutions of the Reynolds Averaged Navier-Stokes (RANS) equations and, to a lesser extent, with Large-Eddy Simulations (LES) techniques (Caciolo et al. 2012). The relatively high Reynolds number, with length scales on the order of several meters and velocities of several tens of meters per second, makes the current use of direct numerical simulations (DNS) almost unfeasible nowadays, due to the extremely high computational cost (Yerragolam et al., 2020; Yang et al., 2021). In addition, the typical forced ventilation strategies encountered in real scenarios, which include free and/or wall jets interacting with thermal stratification and buoyancy effects, produce very different turbulence levels. In turn, this results in, different turbulent length and time scales, in different locations of the room, which is usually characterized by complex geometry (furniture, persons…) and complex boundary conditions (windows, heaters, fans...). The assessment of the performance of RANS and LES approaches has been analyzed by comparing the numerical predictions with experiments (Bournet and Boulard 2010; Caciolo et al. 2012; Villafruela et al., 2013; Gilani et al. 2016; van Hoof et al., 2017). This comparison is often influenced by the finite number of measurements that can be obtained experimentally and by the uncertainty of the measurements themselves and of the boundary conditions.

This paper presents and discusses extensive comparisons of numerical simulations of the flow and particle dispersion in a prototypical room. These simulations have been performed by different research groups in the framework of an international CFD challenge. The goal of this collaborative study is to assess the performance of computationally efficient turbulence modeling techniques, specifically those based on LES, SAS, and RANS simulations, within a well-defined and controlled flow configuration. We have selected a simplified flow setup that permits the use of DNS, enabling us to obtain comprehensive reference data on turbulent flow and particle dispersion. These data serve as a benchmark for comparison with the LES, SAS, and RANS simulation results. We have considered the enclosed turbulent natural convection flow generated by imposing a temperature difference on two pairs of horizontal and vertical walls of a room-size cubical cavity.

DNS of turbulent natural convection flows in cubical enclosures have been performed for different combinations of heated and cooled walls. In particular, turbulent Rayleigh-Bénard convection (Demou and Grigoriadis, 2019, Vasiliev et al., 2019, Delort-Laval et al., 2022) and the turbulent free convection generated in the side-heated cubical enclosure (Tric et al., 2000; Salat et al., 2004; Kalilainen et al., 2016; Dehbi et al., 2017; Wang et al., 2017) have been extensively investigated. Other combinations of heated and cooled walls include the mixed cavity free convection, with simultaneously imposed vertical and horizontal temperature gradients (Hanjalić and Vasić, 1993; Teimurazov et al. 2021). In this particular flow configuration, the orientation and the direction of fluid rotation within the large-scale circulation are fixed and determined by the thermally active vertical walls. This is in contrast to the classical Rayleigh-Bénard problem in a cubic cavity, heated from below and cooled from above, with adiabatic vertical walls. In this scenario, the large-scale circulation changes orientation with a relatively low frequency (Soucasse et al., 2019, Maity et al., 2022) and this introduces a time scale which is much longer than the characteristic time scales associated with the instantaneous turbulent flow structures. Numerical simulations of the laminar and turbulent mixed cavity natural convection have been reported in the range $10^5 \leq Ra \leq 5\times10^8$ by Fabregat and Pallares (2020) and at $Ra = 3.6\times10^9$ by Lavrinenko et al., (2023), where Ra is the Rayleigh number, the ratio of buoyancy and thermal diffusivity. At such high *Ra*, the thermal boundary layers on the horizontal walls are fully turbulent, while those attached to the thermally active vertical walls, although unsteady, are essentially laminar. We selected this flow, for which DNS can be obtained, as a prototypical indoor turbulent natural convection flow in a generic room to analyse the turbulent dispersion of particle tracers.

This paper is structured as follows: Section 2 describes the physical model of the mixed cavity configuration, outlines the organization and the challenge framework and indicates the metrics used for the comparison of the results of the different participants. Section 3 is devoted to the presentation and discussion of the results. Finally, conclusions and recommendations are outlined in Section 4.

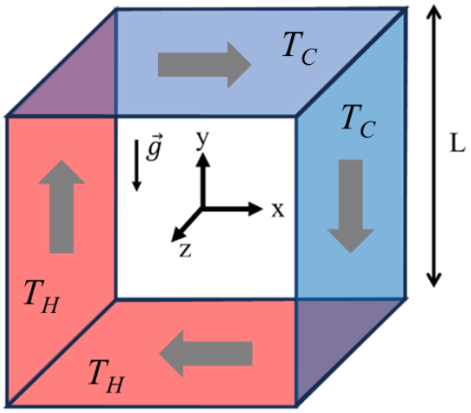

Figure 1. Sketch of the cubical cavity and the coordinates. Hot/Cold walls are indicated in red/blue. The arrows show the rotation of the large-scale flow circulation.

2. PROBLEM DEFINITION AND CHALLENGE FRAMEWORK

2.1. Physical model

We consider the dispersion of particles in a three-dimensional turbulent natural convection flow enclosed in a room-sized cubical cavity. The physical model of the cubical cavity, with dimension $L = 2.5$ m, and the Cartesian coordinates adopted are shown in Figure 1. The origin of coordinates is located at the center of the cavity. The bottom wall and a vertical wall are kept at a constant and uniform temperature (T_H), larger than the constant and uniform temperature of the top and the vertical opposed wall (T_C). The other two vertical sidewalls are considered perfectly adiabatic. The fluid is air at ambient temperature ($T_0 = (T_H + T_C)/2$) and pressure. The physical properties of the fluid (see Table 1) are assumed to be constant with temperature except for the density, which varies linearly with temperature ($\rho = \rho_0[1 - \beta(T - T_0)]$). This dependence is only considered in the buoyancy term according to the Boussinesq approximation. Viscous heating and radiation heat transfer are neglected.

Ra	Pr	ρ_0 (kg/m^3)	μ (Pa·s)	k (W/m K)	C_p (J/kg K)	β (K^{-1})	L (m)	T_H (°C)	T_C (°C)	T_0 (°C)
3.6×10^9	0.7	1.161	1.85×10^{-5}	2.64×10^{-2}	1007	3.33×10^{-3}	2.50	28.11	25.57	26.84

Table 1. Physical properties and parameters of the problem.

The values of the Rayleigh number ($Ra = g\beta(T_H - T_C)L^3/\nu\alpha$) and the Prandtl number ($Pr = \nu/\alpha$) are 3.6×10^9 and 0.7, respectively. In the definitions of these non-dimensional parameters, $\alpha = \frac{k}{\rho_0 C_p}$ is the thermal diffusivity. The flow at lower Rayleigh numbers in this configuration has been analyzed by Fabregat and Pallares (2020) and some quantities at this high Rayleigh number are reported in Lavrinenko et al., (2023) and Lavrinenko et al., (2024).

We consider the unsteady dispersion of two clouds of solid spherical particles released when the turbulent natural convection flow is statistically fully developed. The initial shape of the clouds is spherical, with dimension $D_c = 0.5$ m ($D_c^* = \frac{D_c}{L} = 0.2$), and particle distribution inside the clouds is uniform. Cloud#1 is located near one of the bottom corners of the cavity, where the hot horizontal and vertical walls meet, and the center of Cloud#2 is located in the geometrical center of the cavity. The coordinates of the centers of the two clouds, with respect to the coordinates shown in Fig. 1 are $x_{c1} = y_{c1} = z_{c1} = -0.4L$ and $x_{c2} = y_{c2} = z_{c2} = 0$, respectively.

The particles are assumed to be perfectly spherical with a constant diameter ($d_p = 0.5$ μm) and with density $\rho_p = 1350$ kg/m^3. This relatively small diameter has been selected to minimize the gravitational settling of the particles. Participants were asked to compute the particle dispersion using a Lagrangian method under the one-way coupling hypothesis and according to the following requirements: The equations of particle motion had to be integrated at least during $t^* = t\frac{\alpha\sqrt{Ra}}{L^2} = 150$ non-dimensional time units ($t \approx 700$ s) with a proper time integration step; the number of particles in each cloud had to be larger than 1000. According to the simulations by Lavrinenko et al., (2023), for the flow conditions considered, only a few particles are expected to reach the wall and, by default, for these events, a perfect elastic rebound can be assumed.

2.2. Challenge framework

BuildWind SRL	Belgium
CERFACS	France
Eurecat	Spain
Federal University of Uberlândia - Westmont College	Brazil - USA
FS Dynamics Portugal	Portugal
Heilbronn University of Applied Sciences	Germany
Otto von Guericke University of Magdeburg	Germany
RMIT University - The University of Sydney	Australia
Universitat Politècnica de Catalunya	Spain
University of Birmingham	UK
University of Erlangen Nuremberg- University of Maribor	Germany - Slovenia
University of Maribor	Slovenia

Table 2. Affiliation of the participating teams. Alphabetical order.

The objective of the challenge is to assess the validity of using a computationally affordable turbulence model to reproduce both the flow dynamics and the dispersion of the aerosol cloud in an idealized indoor environment.

The Challenge was officially announced on October 2, 2023. A flyer, included in the Supplementary Material, was distributed to a mailing list of approximately 400 recipients. This list comprised researchers within the organizers' network, supplemented with emails gathered from journal publications focused on numerical simulations of turbulent natural convection flows and particle dispersion. We received expressions of interest from 30 teams. These teams were provided with the Instructions document, available in the Supplementary Material. By the submission deadline of May 1, 2024, data had been received from 12 teams, contributing a total of 15 simulations. Each team's results were presented and discussed during an online workshop held on June 20, 2024. Table 2 provides an affiliation-ordered list of participants, representing academic institutions, research centers and engineering firms.

To prevent misleading collaborations among participants, the challenge was organized as a blind test. Participants were unaware of the other teams until after the data submission deadline, and file exchanges between participants and organizers were conducted via private Google Drive folders for each team. The DNS data published by Fabregat and Pallares (2020) and by Lavrinenko et al., (2023), which were made freely available to the teams during the challenge, were recommended as benchmarks. Participants were required to submit data in ASCII or VTK formats to facilitate post-processing with the open-source multi-platform software ParaView (ParaView, 2024).

Table 3 summarizes the most important information from the simulations submitted. In addition, the specific details of each turbulence models used and of the models of the different terms of the particle force balance are included as supplementary material. The last column of Table 3 identifies each specific simulation with a code with two letters. The randomized first letter (from A to L) identifies the team, while the second corresponds to the turbulent modelling used (namely L for Large-Eddy Simulation, H for hybrid URANS-LES methods, S for Scale-Adaptive Simulation, U for URANS-based simulation or R for RANS-based simulation). Three teams (F, H and L) performed the simulations with commercial codes, six teams (B, C, D, G, I and K) with the open-source OpenFOAM solver and three teams (A, E and J) used their own in-house solvers. All the simulations were carried out with finite volume solvers, except for the in-house solvers used by teams A and J, which are based, respectively, on finite element and finite difference techniques for the spatial discretization of the governing equations. The set of fifteen simulations comprises three Large-Eddy Simulations, four hybrid LES-RANS simulations, two Scale-Adaptive Simulations, three URANS-based simulations and three RANS-based simulations. The teams were instructed to conduct a grid independence test to determine the appropriate mesh resolution. The selected grids, along with the minimum and maximum grid spacings, are reported in Table 3. The value of y^+ corresponding to the minimum distance of the nodes to the horizontal walls, where the boundary layers are turbulent, is 0.3 for the DNS grid ($\Delta x_{min}=1.6\times10^{-4}L$). For reference, $\Delta x_{min}=5\times10^{-4}L$ corresponds to $y^+=0.9$ and $\Delta x_{min}=10^{-3}L$ to $y^+=1.8$. All teams employed hexahedral elements for their meshes, except for team A, which adopted a grid composed of tetrahedra with two layers of prisms attached to the walls. The LES of team L used a grid of 7 million nodes, while the other two LES teams employed finer grids, with team A using 91 million nodes and team J using 64 million nodes. The number of elements of the meshes for the hybrid simulations are about one order of magnitude smaller and range between 2 and 8 million nodes. SAS were performed with grids between 3 and 4 million nodes. The grids selected for URANS and RANS-based simulations generally contain a moderate number of elements, ranging from 0.03 to 4.8 million nodes, except for the simulation of team F, which used 21.2 million nodes. Non-uniform grids stretched towards the

walls, were used by all teams, except team J, which used a uniform grid. The minimum non-dimensional grid spacings, scaled with the size of the cavity, located near the walls are of order 10^{-4}-10^{-3} and most of the non-dimensional maximum grid spacings, located near the center of the cavity are of order 10^{-2}, with the exception of teams J and H, which used minimum grid sizes of order 10^{-3}. These minimum grid spacings compare reasonably well with the DNS estimations of the time and wall-averaged temperature boundary layer thickness ($\delta/L = (2Nu)^{-1}$), see for example Scheel and Schumacher, 2014) for the vertical ($Nu_v = 78, \delta_v/L = 6.4 \times 10^{-3}$) and horizontal walls ($Nu_h = 112, \delta_h/L = 4.4 \times 10^{-3}$). Also good is the estimation of the Kolmogorov length scale ($\eta/L \approx 10^{-3}$) for a Rayleigh-Bénard flow at $Ra = 3.6 \times 10^9$ and $Pr = 0.7$ (Scheel et al., 2013). The temporal discretization of the governing flow equations for the LES, performed with the finer grids, is explicit (3rd order for team A and 2nd order for team J), while for the hybrid, SAS and URANS simulations the discretization is implicit. The time steps employed by the different teams range from 3.5×10^{-5} s, for the finest grid, to 2×10^{-1} s for the coarser grids. The minimum number of particles per cloud was set by the organizers according to preliminary numerical tests that showed that the particle dispersion rate metrics, which are presented and described below, in subsection 2.3, were essentially independent for clouds with 1000 or more particles. The gravity and drag forces were considered by all the teams in the particle force balance. In any case, the terminal velocity of the particles is 10 μm/s and consequently gravity is not expected to play a significant role in the dispersion which is monitored during 700 s. The lift force and thermophoresis, included in the particle force balance by some teams, are also expected to have a very limited effect, because of the relatively small density ratio between the fluid and the particles and the reduced values of the temperature gradients where the particle dispersion takes place (i.e., outside the thin thermal boundary layers near the thermally active walls). Random walk models are incorporated in the motion of the particles to account for the effect of turbulence fluctuations in simulations using SAS, URANS or RANS.

Team	Code	Turbulence	Spatial discretization	Grid	$\Delta x_{min}/\Delta x_{max}$	Temporal discretization*	#particles /cloud	Particle forces	Code
A	AVBP (Schønfeld and Rudgyard, 1999. Duchaine et al. 2021)	LES: WALE (Pr_{SGS}=0.6)	Finite element. 3rd order	91M tetrahedral/ prism	2.5×10^{-3} 2.0×10^{-2}	Explicit. 3rd order $\Delta t_f = \Delta t_p = 3.5\times10^{-5}$ s	2000	Drag Gravity	A-L
B	OpenFOAM 2106 (Weller et al. 1998)	URANS: k-ε	Finite volume. 1st order upwind	0.4M hexahedral (75×75×75)	6.0×10^{-3} 6.2×10^{-2}	Implicit. 1st order $\Delta t_f = \Delta t_p = 10^{-1}$ s	1440	Drag Gravity Random-Walk	B-U
C	OpenFOAM 11 (Weller et al. 1998)	SAS: k-ω SST	Finite volume. 2nd order	3.2M hexahedral (147×147×147)	4.7×10^{-4} 1.3×10^{-2}	Implicit. 1st order $\Delta t_f = 2\times10^{-2}$ s $\Delta t_p = 5\times10^{-3}$ s	1021	Drag Gravity Random-Walk	C-S
D	OpenFOAM 2112 (Weller et al. 1998)	RANS: k-ω	Finite volume. 2nd order	4.8M hexahedral (168×168×168)	2.4×10^{-3} 2.0×10^{-2}	$\Delta t_p = 5\times10^{-3}$ s	1000	Drag Lift Gravity Random-Walk	D-R
E	UNSCYFL3D (Velasco et al. 2022)	DES: SST	Finite volume. 2nd order	2.0M hexahedral (125×125×125)	8.0×10^{-4} 5.6×10^{-2}	Implicit. 2nd order $\Delta t_f = \Delta t_p = 10^{-1}$ s	55000	Drag Gravity Thermo-phoresis Random-Walk	E-H
		URANS: SST							E-U
F	STAR-CCM+ 2022.1.1 (STAR-CCM+, 2024)	RANS: k-ω SST	Finite volume. 1st order	21.2M hexahedral (276x276x276)	2.0×10^{-3} 1.2×10^{-2}	$\Delta t_p = 4\times10^{-2}$ s	1500	Drag Gravity	F-R
G	OpenFOAM 11 (Weller et al. 1998)	DES: k-ω SST	Finite volume. 2nd order	4.2M hexahedral (161×161×161)	5.1×10^{-4} 1.3×10^{-2}	Implicit. 1st order $\Delta t_f = \Delta t_p = 10^{-2}$ s	10000	Drag Gravity Random-Walk	G-H
		SAS: k- ω SST							G-S
H	Ansys Fluent 2024R1 (Ansys Fluent, 2024)	SBES using LES: WALE, RANS: k-ω SST (Pr_{SGS}=0.85)	Finite volume. 2nd order	8.0M unstructured hexahedral	4.0×10^{-4} 6.4×10^{-3}	Implicit. 2nd order $\Delta t_p = 10^{-2}$ s	1000	Drag Gravity	H-H
I	OpenFOAM 11 (Weller et al. 1998)	DES: k-ω SST	Finite volume. 2nd order	1.0M hexahedral (100x100x100)	2.8×10^{-4} 1.7×10^{-2}	Implicit. 1st order (max. Δt =0.017 s)	2500	Drag Gravity Random-Walk	I-H
J	MultiFlow3D (Fraga et al. 2016. Monka et al. 2023)	LES: Smagorinsky	Finite difference 2nd order	64M hexahedral (400x400x400)	2.5×10^{-3} 2.5×10^{-3}	Explicit. 2nd order $\Delta t_f = \Delta t_p = 5\times10^{-3}$ s	1500	Drag Gravity Lift Added mass	J-L
K	OpenFOAM 8 (Weller et al. 1998)	RANS: k-ε	Finite volume. 2nd order	0.03M (prisms + unstructured hexahedra)	5.5×10^{-3} 4.0×10^{-2}	$\Delta t_p = 10^{-1}$ s	1464	Drag Gravity Lift	K-R
L	STAR-CCM+ 2021.3 (STAR-CCM+, 2024)	LES: WALE (Pr_{SGS}=0.7)	Finite volume. 2nd order	7M hexahedral (191x191x191)	8.0×10^{-4} 7.2×10^{-3}	Implicit. 2nd order $\Delta t_f = 1.6\times10^{-2}$ s	5016	Drag Gravity Pressure gradient	L-L
		URANS: k-ε		2M hexahedral (126x126x126)	8.0×10^{-4} 1.8×10^{-2}	Implicit. 2nd order $\Delta t_f = 10^{-1}$ s			L-U

Table 3. Summary of the simulations details.

(*) Δt_f: Time step for the flow equations. Δt_p: Time step for the particle equations.

2.3. Metrics for the comparison of the results

Participants were asked to submit the surface averaged Nusselt numbers on the vertical (Nu_v) and horizontal (Nu_h) walls. These are defined as $Nu_v = \langle q_v^{"} \rangle L/k(T_H - T_C)$ and $Nu_h = \langle q_h^{"} \rangle L/k(T_H - T_C)$, where $\langle q_v^{"} \rangle$ and $\langle q_h^{"} \rangle$ are the surface averaged wall heat fluxes on the vertical and horizontal walls, respectively.

The deviations, with respect to DNS, of the predictions of the velocity, temperature and turbulence kinetic energy profiles along the wall bisectors of the vertical symmetry plane of the cavity ($z = 0$), were evaluated by computing the root mean squared differences. First, we interpolated the data submitted by the different teams onto the DNS mesh and computed the root mean squared values as

$$\sigma_\phi = \sqrt{\frac{\sum_{i=1}^{i=N^{DNS}} \left(\phi_i^X - \phi_i^{DNS}\right)^2}{N^{DNS}}} \quad (1)$$

where σ_ϕ is the rms for the quantity ϕ, which can correspond to velocity, temperature or turbulence kinetic energy, ϕ_i^X is the data of team X interpolated onto the DNS mesh, ϕ_i^{DNS} is the data corresponding to the DNS profiles and N^{DNS} is the number of grid points along the wall bisectors used in the DNS.

The square of the average distance, or separation, of all possible particle pairs has been used to monitor the dispersion of the two particle clouds. We defined three quantities, given in Equations (2) to (4) to measure, respectively, the three-dimensional dispersion within the cavity (D_{xyz}^{*2}), the dispersion in the plane of rotation of the large-scale circulation (D_{xy}^{*2}) and the dispersion along the z-direction (D_z^{*2}), that corresponds to the direction of the main alignment of the rotation vector of the large-scale flow (see Fig. 1).

$$D_{xyz}^{*2} = \frac{1}{N}\sum_{i,j}\left(\left[x_i^* - x_j^*\right]^2 + \left[y_i^* - y_j^*\right]^2 + \left[z_i^* - z_j^*\right]^2\right) \quad (2)$$

$$D_{xy}^{*2} = \frac{1}{N}\sum_{i,j}\left(\left[x_i^* - x_j^*\right]^2 + \left[y_i^* - y_j^*\right]^2\right) \quad (3)$$

$$D_z^{*2} = \frac{1}{N}\sum_{i,j}\left(\left[z_i^* - z_j^*\right]^2\right) \quad (4)$$

In Eqs. (2) to (4), N is the total number of possible particle pairs, which is related to the total number of particles in each cloud, n, as

$$N = \sum_{k=1}^{n-1}(n-k) = \frac{n(n-1)}{2}. \tag{5}$$

According to the definitions of Eqs. (2) to (4)

$$D_{xyz}^{*2} = D_{xy}^{*2} + D_z^{*2}. \tag{6}$$

The limiting dimensional values of the mean squared distance, D_{xyz}^2, corresponding to a perfectly uniform distribution of particles in a cubical box, with dimension L, can be computed as

$$D_{xyz}^2(t\to\infty) = \frac{1}{L^6}\int_{z_2=-L/2}^{z_2=L/2}\int_{y_2=-L/2}^{y_2=L/2}\int_{x_2=-L/2}^{x_2=L/2} \left\{\int_{x_1=-L/2}^{x_1=L/2}\int_{y_1=-L/2}^{y_1=L/2}\int_{x_1=-L/2}^{x_1=L/2}[\langle(x_1-x_2)^2+(y_1-y_2)^2+(z_1-z_2)^2\rangle\, dx_1\, dy_1\, dz_1]\right\} dx_2\, dy_2\, dz_2 = \frac{L^2}{2}. \tag{7}$$

Similarly, $D_{xy}^2(t\to\infty) = \frac{L^2}{3}$ and $D_z^2(t\to\infty) = \frac{L^2}{6}$.

Initially the particles are released in spherical clouds, with diameter D_c, and particle distribution is uniform. The corresponding dimensional value of D_{xyz}^2 can be computed as

$$D_{xyz}^2(t=0) = \frac{1}{\left(\frac{\pi D_c^3}{6}\right)^2}\int_{\varphi_2=0}^{\varphi_2=2\pi}\int_{\theta_2=0}^{\theta_2=\pi}\int_{r_2=0}^{r_2=D_c/2} \left\{\int_{\varphi_1=0}^{\varphi_1=2\pi}\int_{\theta_1=0}^{\theta_1=\pi}\int_{r_1=0}^{r_1=D_c/2}[\langle(r_1\sin\theta_1\cos\varphi_1 - r_2\sin\theta_2\cos\varphi_2)^2 + (r_1\sin\theta_1\sin\varphi_1 - r_2\sin\theta_2\sin\varphi_2)^2 + (r_1\cos\theta_1 - r_2\cos\theta_2)^2\rangle\, r_1^2\sin\theta_1\, dr_1\, d\theta_1\, d\varphi_1]\right\} r_2^2\sin\theta_2\, dr_2\, d\theta_2\, d\varphi_2 = \frac{3D_c^2}{10} \tag{8}$$

Similarly, $D_{xy}^2(t=0) = \frac{D_c^2}{5}$ and $D_z^2(t=0) = \frac{D_c^2}{10}$

These limiting dimensional values can be used to bound the non-dimensional values of the mean squared average distances between 0 and 1.

$$D_{xyz}^{**2} = \frac{D_{xyz}^2 - D_{xyz}^2(t=0)}{D_{xyz}^2(t\to\infty) - D_{xyz}^2(t=0)} \quad (9)$$

$$D_{xy}^{**2} = \frac{D_{xy}^2 - D_{xy}^2(t=0)}{D_{xy}^2(t\to\infty) - D_{xy}^2(t=0)} \quad (10)$$

$$D_{z}^{**2} = \frac{D_{z}^2 - D_{z}^2(t=0)}{D_{z}^2(t\to\infty) - D_{z}^2(t=0)} \quad (11)$$

In this case, the following inequality holds for the non-dimensional distances, $D_{xyz}^{**2} \neq D_{xy}^{**2} + D_{z}^{**2}$.

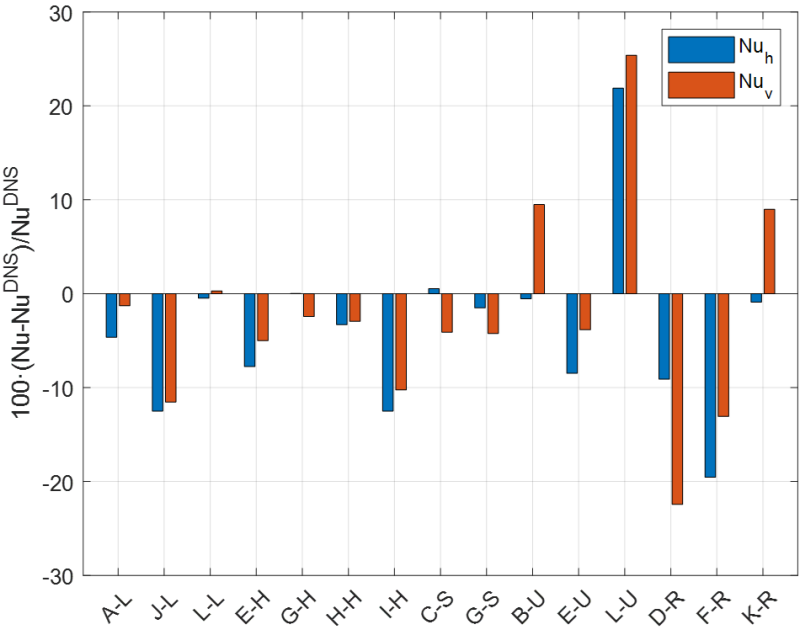

Figure 2. Differences in the surface-averaged Nusselt numbers on the horizontal (Nu_h) and vertical (Nu_v) walls.

3. RESULTS AND DISCUSSION

3.1. Flow and heat transfer

Figure 2 shows the differences, expressed as a percentage, of the predictions of the surface averaged Nusselt numbers on the horizontal and vertical walls with respect to the DNS results ($Nu_h^{DNS} = 112, Nu_v^{DNS} = 78$). In general, the predictions obtained with the URANS or RANS approaches show larger deviations (± 25%) than the LES/hybrid or SAS methods (− 12%). The two SAS simulations,

carried out with similar grid resolutions, exhibit differences smaller than 5%. Four of the simulations performed with the LES/hybrid techniques (A-L, L-L, G-H and H-H) also show deviations smaller than 5%. These simulations used, respectively, grids of 91M, 7M, 4.2M and 8M nodes, while the simulations E-H and I-H, with differences larger than 5% were carried out with coarser meshes of 2M and 1M nodes. The LES of team J also show differences larger than 5%, despite the use of a uniform grid with 64M nodes.

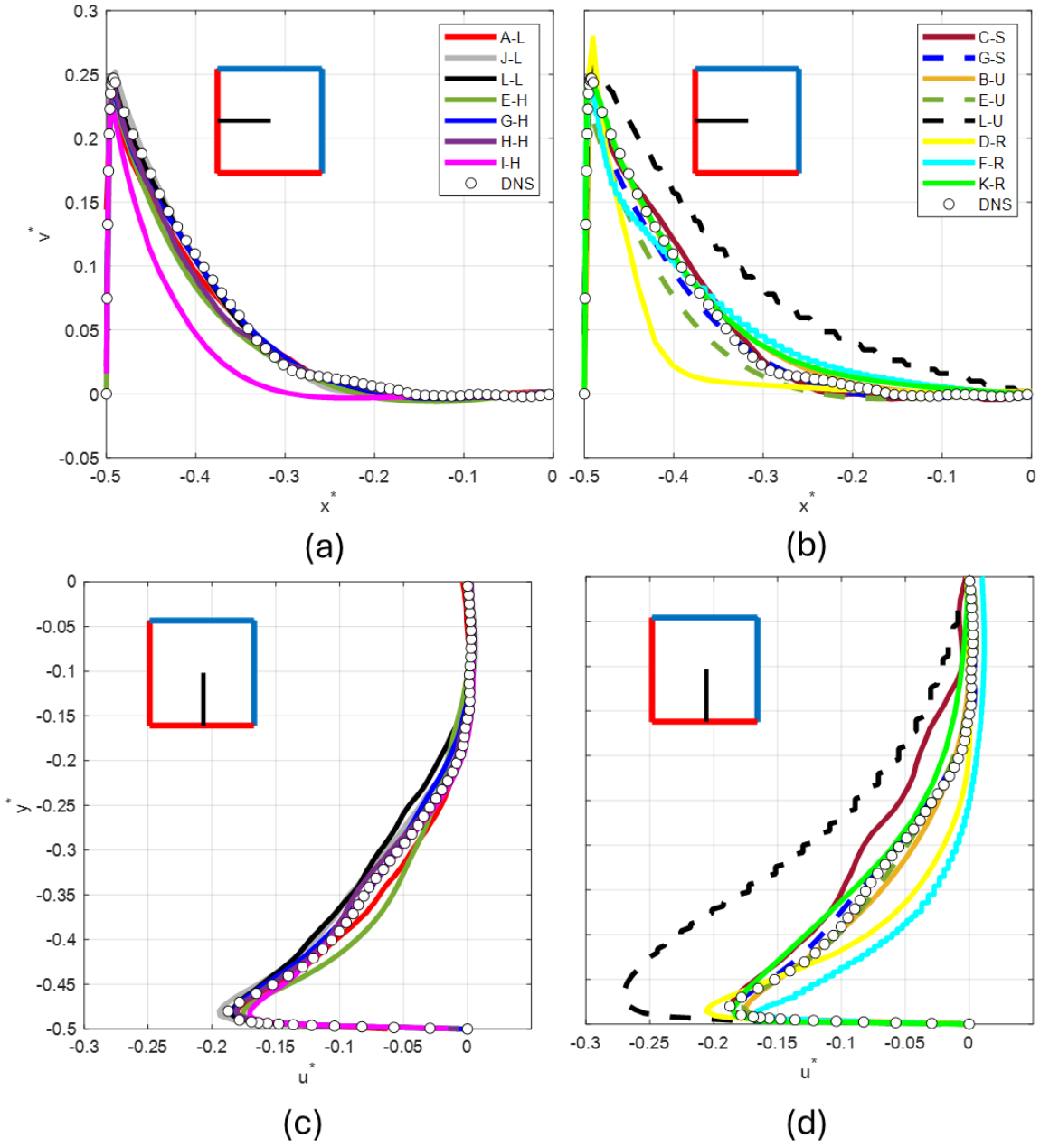

Figure 3. Non-dimensional time-averaged velocity profiles along the horizonal (a and b) and vertical (c and d) bisectors of the vertical symmetry plane of the cavity ($z = 0$).

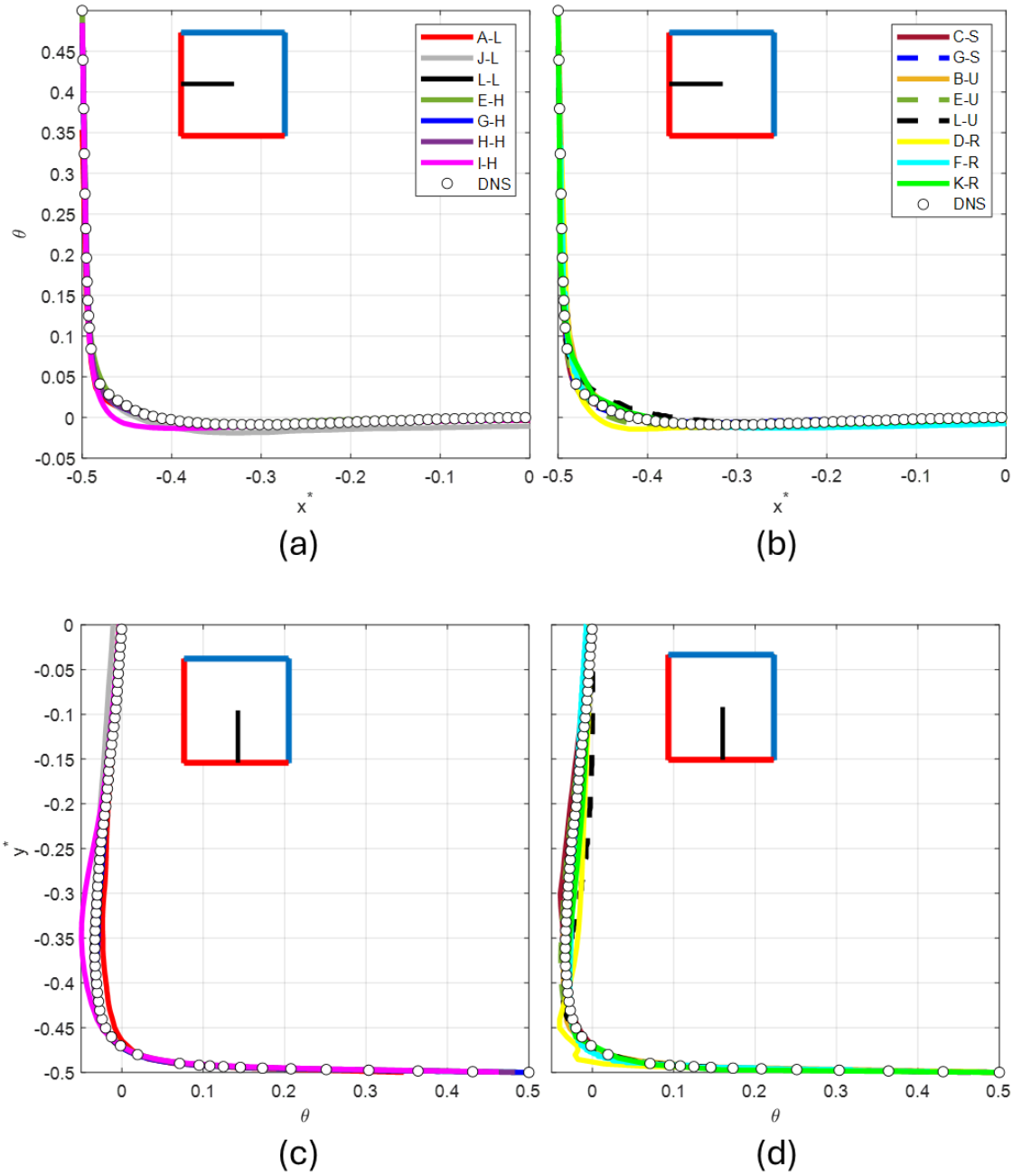

Figure 4. Non-dimensional time-averaged temperature profiles along the horizonal (a and b) and vertical (c and d) bisectors of the vertical symmetry plane of the cavity ($z = 0$).

The time averaged profiles of the non-dimensional velocity, temperature and turbulence kinetic energy along the horizontal and vertical bisectors of the vertical symmetry plane of the cavity are plotted in Figures 3, 4 and 5, respectively. The length, time and temperature scales, used to obtain the non-dimensional variables, are the size of the cavity, L, the convection time, $L^2/\alpha\sqrt{Ra}$, and the temperature increment, $T_H - T_C$ (i.e. $x_i^* = x_i/L$, $u_i^* = u_i L^2/\alpha\sqrt{Ra}$ and $\theta = (T - T_o)/(T_H - T_C)$). The DNS predictions are indicated using symbols and the results of the various teams using lines of

different colors. The profiles of the teams that presented two simulations (E, G and L) are plotted with the same color but with a different line pattern. For clarity we plotted LES/hybrid and SAS/URANS/RANS results separately. Figures 3 and 4, corresponding to the velocity and temperature profiles, respectively, show that, overall, the predictions of the LES/hybrid simulations exhibit less variability and a better agreement with the DNS. An exception is the simulation I-H, performed with a relatively coarse mesh. This simulation shows significant deviations with respect to the DNS in the horizontal velocity profile of Figure 3a and in the temperature profiles of Figures 4a and 4c.

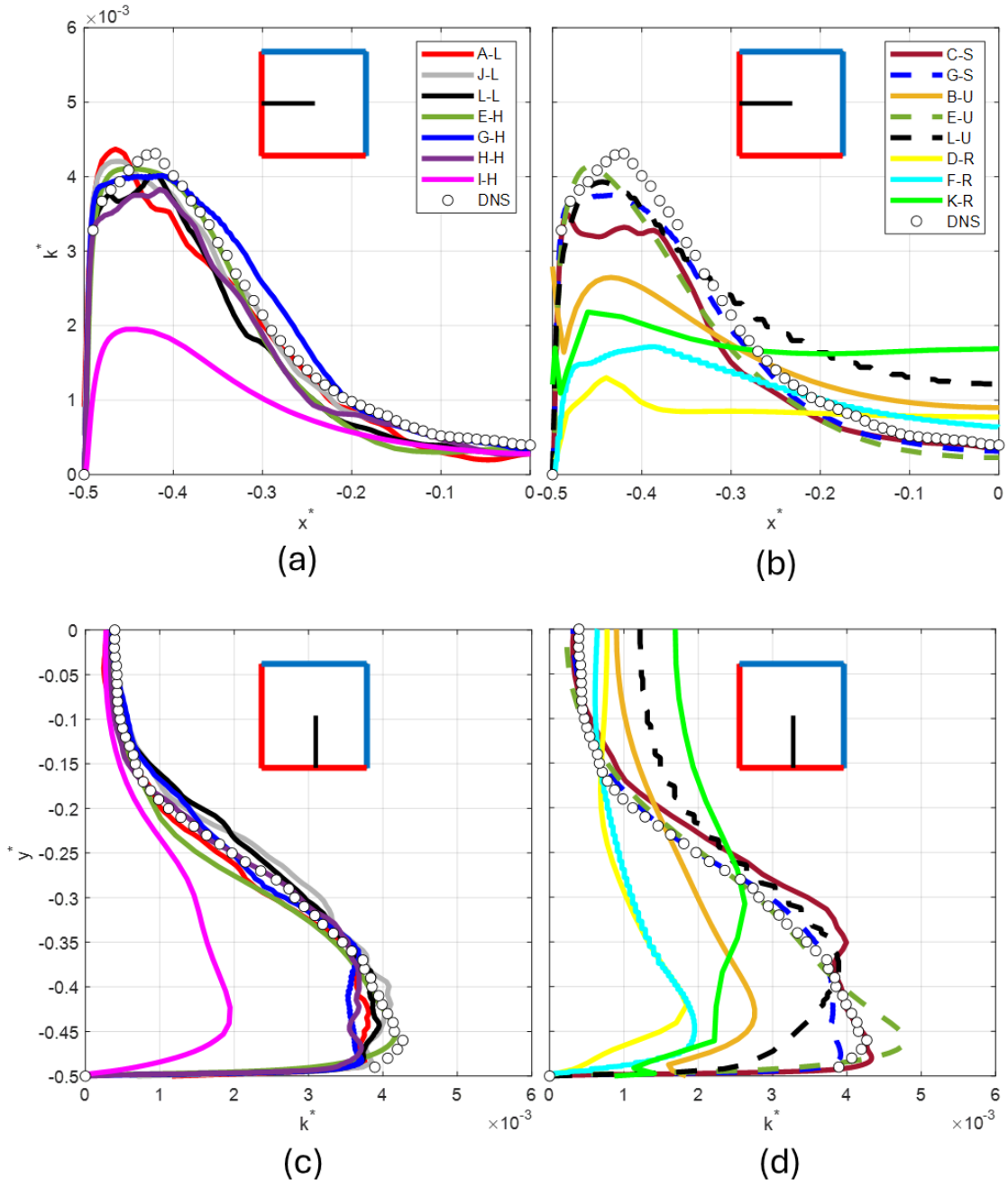

Figure 5. Non-dimensional turbulence kinetic energy profiles along the horizonal (a and b) and vertical (c and d) bisectors of the vertical symmetry plane of the cavity ($z = 0$).

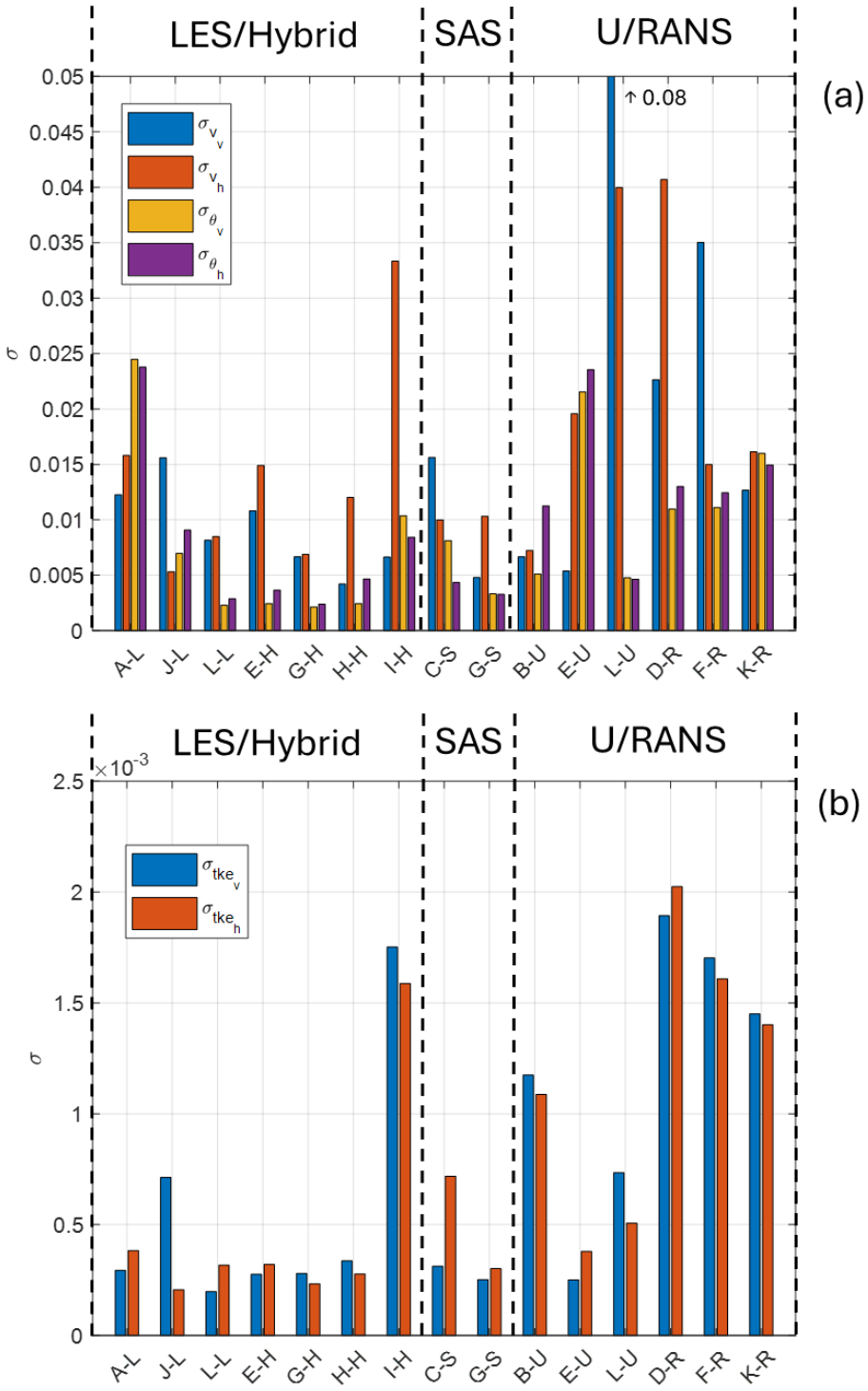

Figure 6. Root mean squared differences, between the different predictions and the DNS, in the profiles of (a) velocity and temperature and (b) turbulence kinetic energy along the horizonal and vertical bisectors of the vertical symmetry plane of the cavity ($z = 0$). The values of the bars above the maximum scale of the vertical axis are indicated.

The turbulence kinetic energy profiles, plotted in Figure 5, also reveal the better overall performance of LES/hybrid techniques. The RANS simulations (Figs. 5b and 5d) tend to underpredict the intensity of the fluctuations near the wall and to overpredict them near the center of the cavity. This is also observed for the URANS simulation B-U, which was carried out with a relatively coarse mesh (0.4M nodes) and a first-order spatial discretization. The SAS results (C-S and G-S) and the URANS, E-U, show predictions that are closer to the DNS. We quantified the departure, from the DNS, of the profiles shown in Figures 3 to 5, by computing the root mean squared differences, defined in Equation (1). The values are plotted in Figure 6a, for the velocity and temperature profiles, and in Figure 6b for the turbulence kinetic energy. These figures summarize the differences already highlighted, when discussing the profiles of the time-averaged velocity, temperature and turbulence kinetic energy. Figure 6b indicates that LES/Hybrid techniques, along with SAS, provide a relatively accurate prediction of the turbulence kinetic energy, especially when compared with the RANS and URANS methods. Exceptions are the simulation I-H, that, as indicated above, exhibits relatively large deviations of the velocity profiles and the URANS simulation E-U, which reproduces well the turbulence kinetic energy (Figs. 5b and 5d) and shows moderate differences with respect to DNS in the velocity and temperature profiles (Figs. 6a).

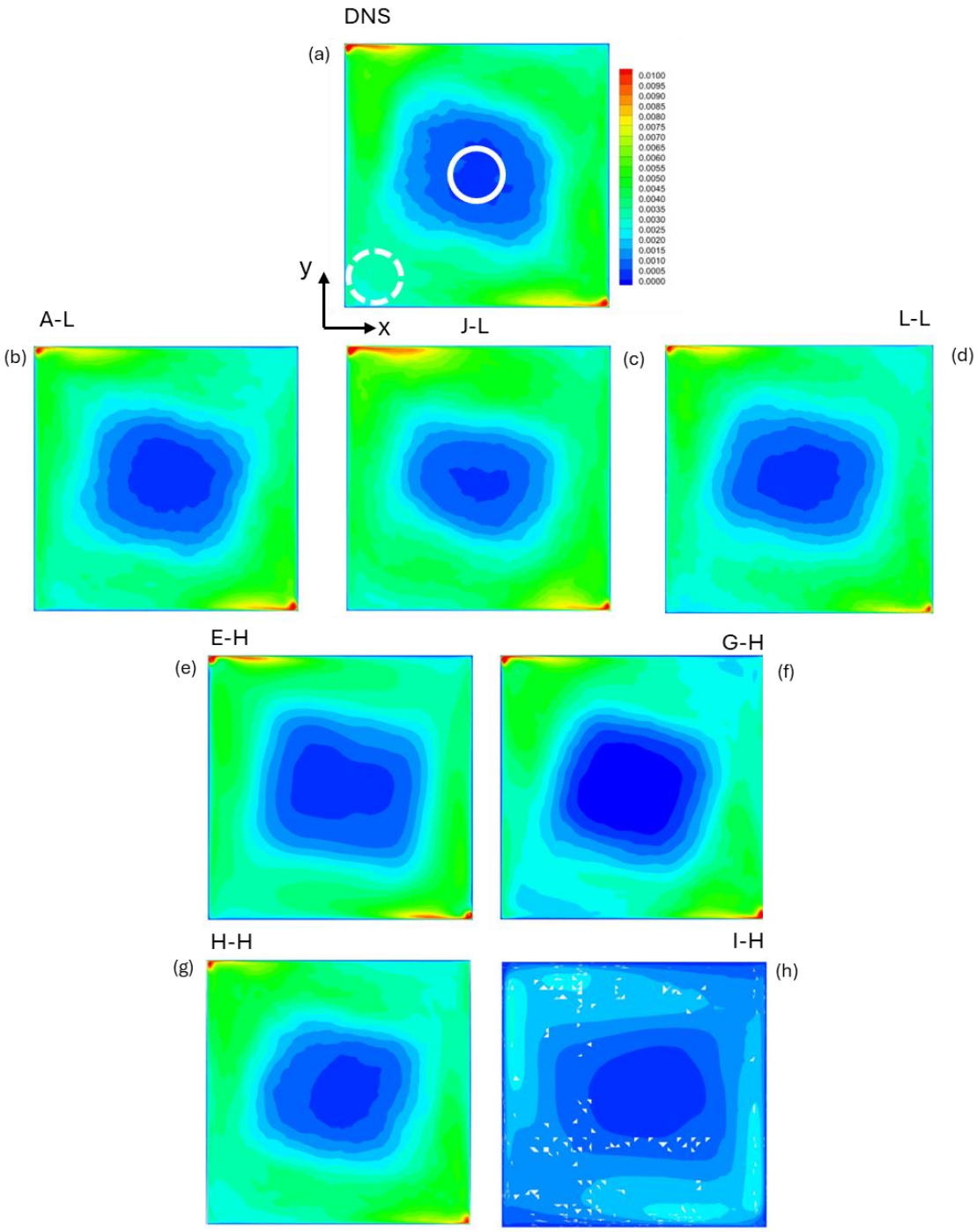

Figure 7. Contours of the turbulence kinetic energy on the vertical symmetry plane of the cavity ($z = 0$).

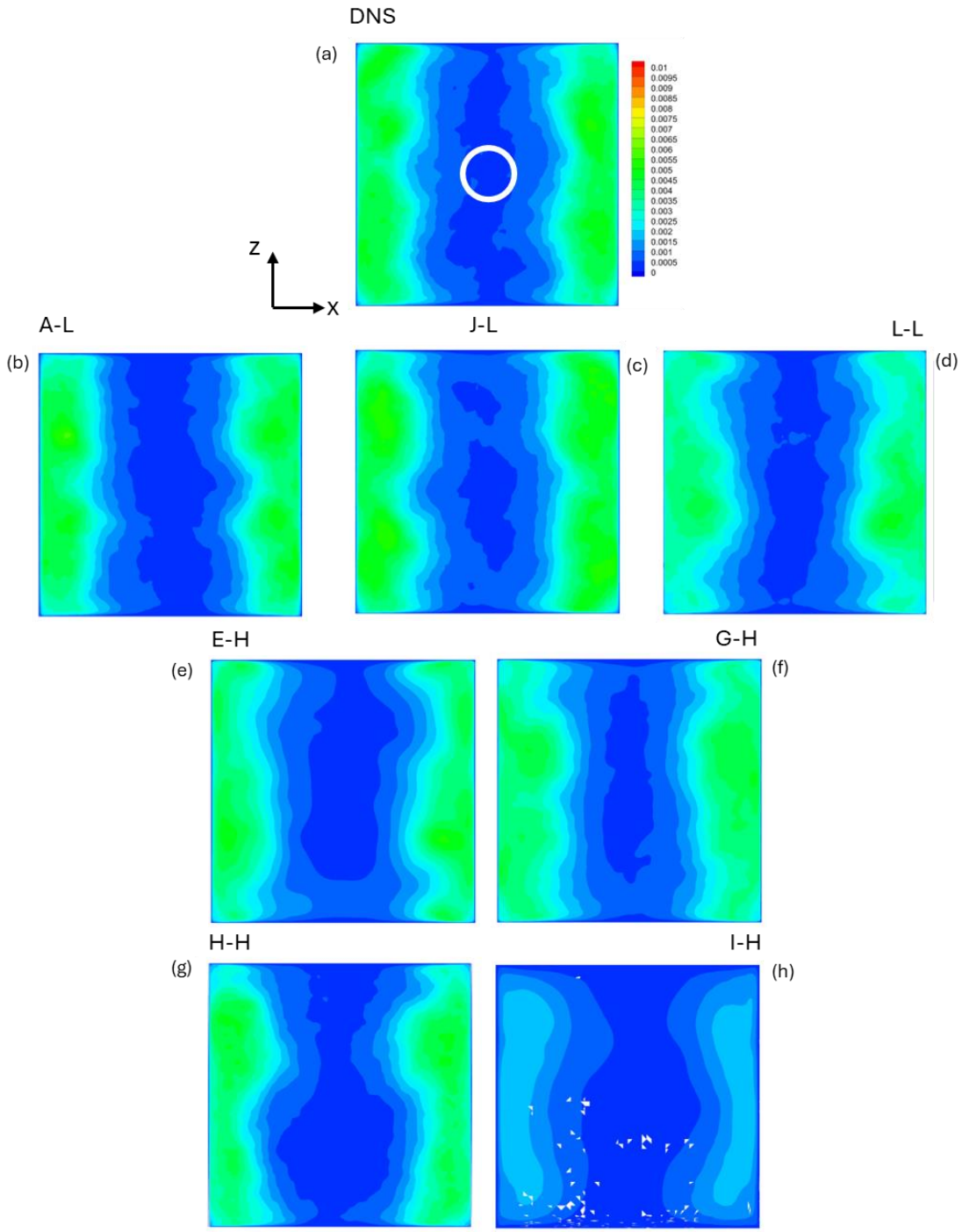

Figure 8. Contours of the turbulence kinetic energy on the horizontal mid plane of the cavity ($y = 0$).

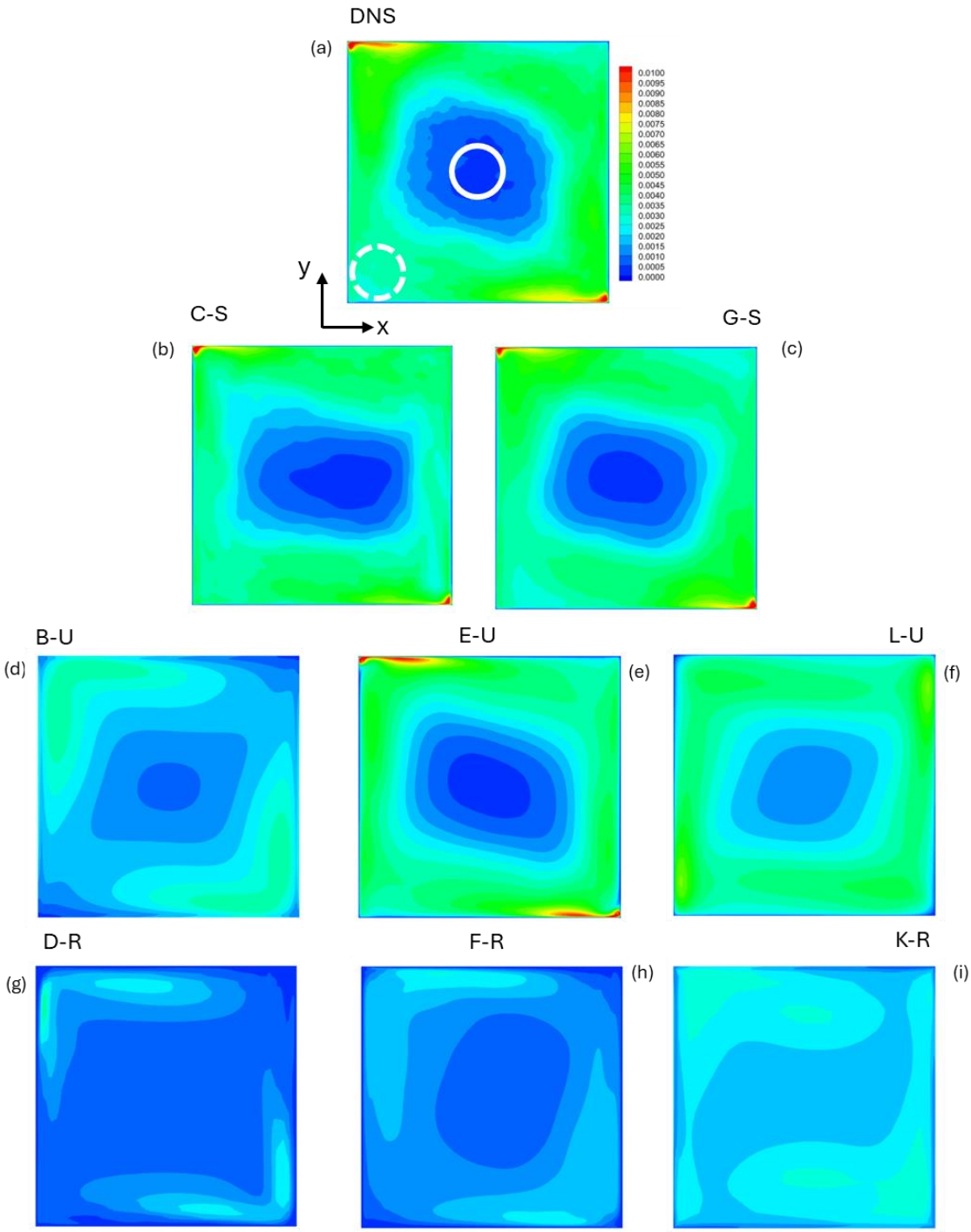

Figure 9. Contours of the turbulence kinetic energy on the vertical symmetry plane of the cavity ($z = 0$).

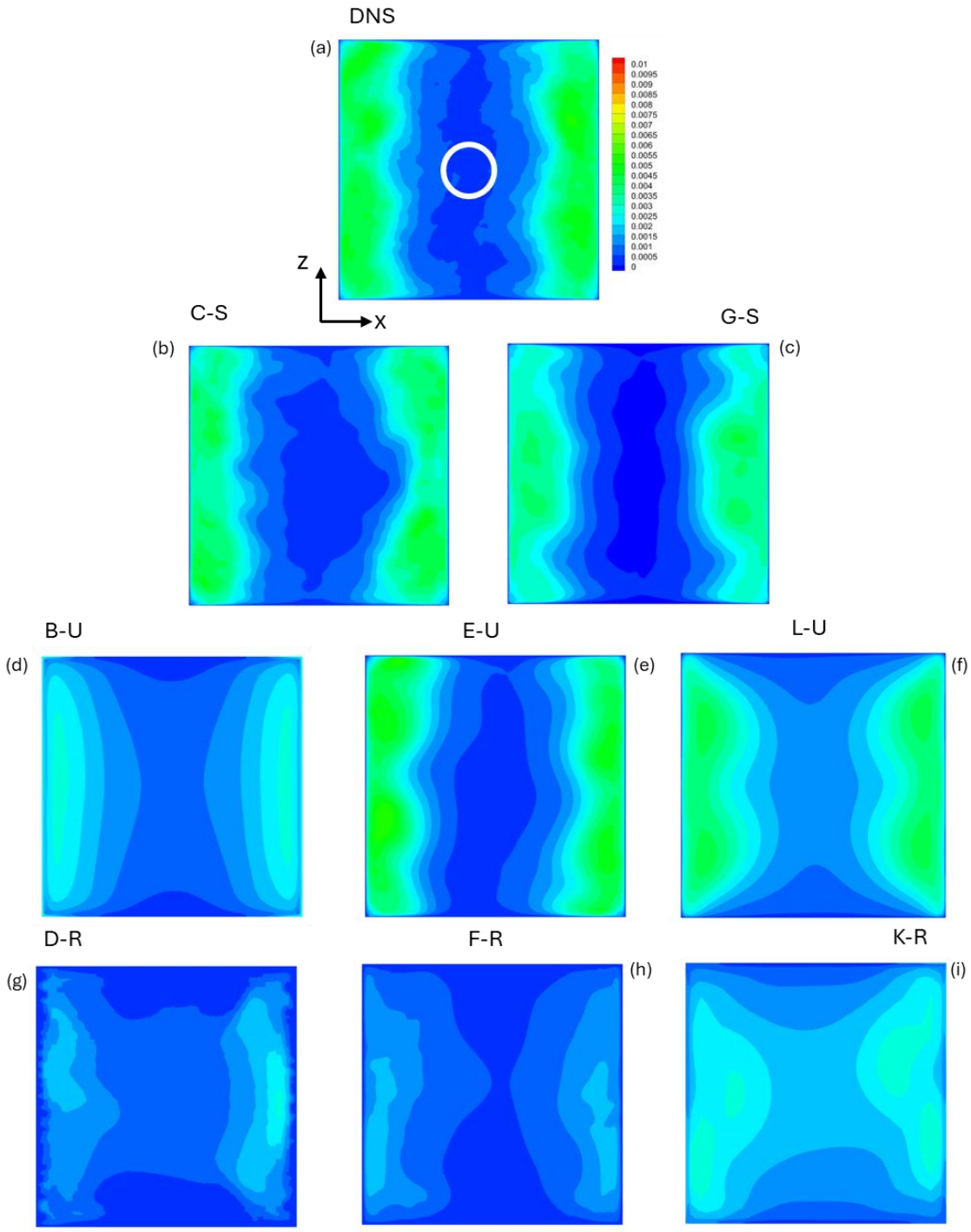

Figure 10. Contours of the turbulence kinetic energy on the horizontal mid plane of the cavity ($y = 0$).

The spatial distribution of turbulence kinetic energy within the cavity plays a crucial role in the three-dimensional dispersion of particle clouds. To illustrate this, the two-dimensional distributions of the turbulence kinetic energy in the vertical symmetry plane of the cavity ($z = 0$) and in the horizontal mid plane ($y = 0$) are plotted in Figures 7 to 10. The initial positions of the particle clouds are indicated by the white circles in Figures 7a, 8a, 9a and 10a, corresponding to the DNS results. Cloud#1 is shown with a dashed line and Cloud#2, with a continuous line. A local minimum in fluctuation intensities can be observed near the center of the cavity. This area is an almost stagnant region in terms of time-averaged behaviour, as indicated by the velocity profiles shown in Figure 3. This is precisely where Cloud#2 originates. The turbulence kinetic energy reaches a local maximum along the path of large-scale flow recirculation, occurring where the time-averaged velocity declines from its peak (located very close to the wall) to a local minimum at the center of the cavity (see Figures 3a and 5a). The turbulence kinetic energy exhibits localized maxima near the top left and bottom right corners of the vertical symmetry plane of the cavity, where the hot and cold walls meet (see for example Figure 7a). The distribution of the turbulence kinetic energy is essentially uniform along the z direction of the cavity, as shown in Figure 8a. This direction is indeed aligned to the rotation axis of the large-scale flow recirculation. As shown in Figure8a, the effect of the adiabatic walls, located at $z = -1/2$ and $z = 1/2$, in the distribution of the turbulence kinetic energy is restricted to areas that are very close to these walls.

Figures 7 and 8 show that, globally, the LES/hybrid techniques provide predictions of the turbulence kinetic energy spatial distributions in the $z = 0$ (Fig. 7) and $y = 0$ (Fig. 8) planes that closely match the DNS benchmark case. However, simulation I-H underpredicts, in general, the level of the fluctuations along the path of the large-scale flow recirculation (see Figs. 7h and 8h). The predictions of the SAS, shown in Figs. 9b, 9c,10b and 10c agree well with the DNS. The contours of the turbulence kinetic energy of the three URANS are plotted in Figures 9d to 9f and 10d to 10f. The simulation E-U (Figs. 9e and 10e), carried out using the k-ω SST model and a grid of 2M cells, agrees with the DNS while the simulation L-U (Figs. 9f and 10f), albeit sharing the same grid resolution, exhibits larger differences with respect to the DNS using the k-ε model. The simulations B-U (Figs. 9d and 10d), also carried out with a k-ε model but on a relatively coarse grid (0.4M cells) shows larger deviations in the distributions of the turbulence kinetic energy with respect to the DNS. The three RANS-based simulations (D-R, F-R and K-R) generally underpredict the levels of the turbulence kinetic energy, as shown in Figures 9g to 9i and 10g to 10i irrespective of the turbulence model (k-ε or k-ω) or grid resolution used (see Table 3). Overall, the evaluation of the local turbulence kinetic energy distribution

is characterized by significantly higher uncertainty in comparison to the velocity and temperature mean profiles.

In summary, the comparative study performed indicates that, in general, SAS methods predict the heat transfer rates and the time-averaged distributions of velocity, temperature, and turbulent kinetic energy as accurately as LES or hybrid techniques, provided the mesh resolutions are comparable.

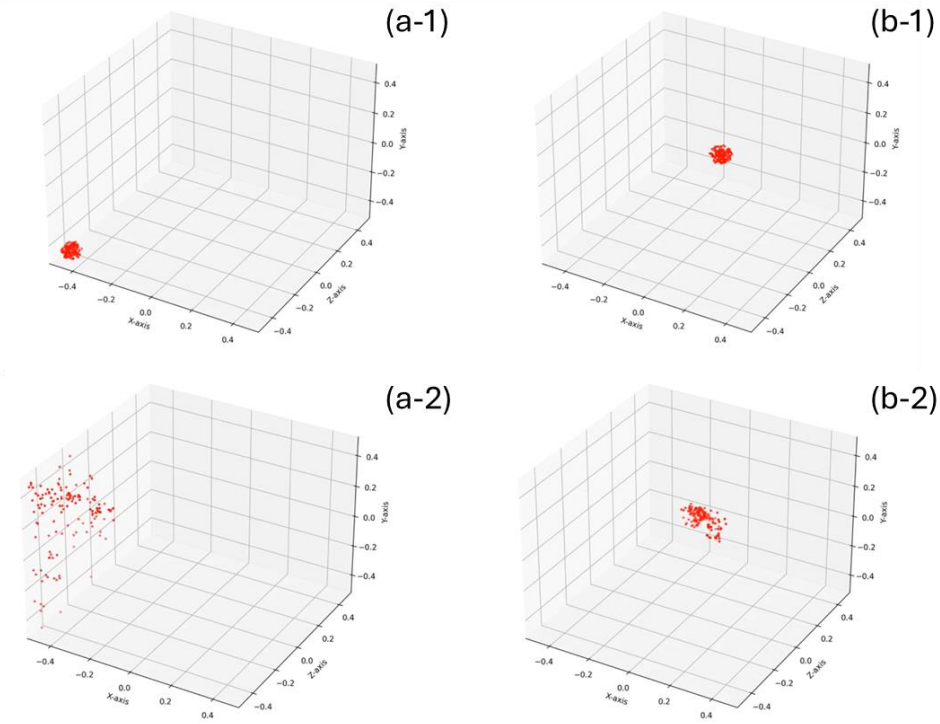

Figure 11. Time evolution of the dispersion of the particles. (a) Cloud#1. (b) Cloud#2. (a-1) and (b-1) correspond to $t^* = 0$ and (a-2) and (b-2) to $t^* = 5$. (Multimedia available online).

3.2. Particle dispersion

Under statistically fully developed flow conditions, we have considered the independent dispersion of two initially spherical particle clouds of identical size. Cloud#1 is released near one corner of the cavity and Cloud#2, in the center of the cavity (see Fig. 11, Multimedia available online). It can be seen that Cloud#1 is rapidly advected by the large-scale recirculation while particles belonging to Cloud#2 are progressively dispersed within the nearly stagnant center of the cavity and eventually are transported by the large-scale recirculation near the vertical or horizontal thermally active walls.

The time evolutions, predicted by the DNS, of the non-dimensional mean squared values of the particle separations; D_{xyz}^{**2}, D_{xy}^{**2} and D_{z}^{**2}, defined in Eqs. (9) to (11), are plotted in Fig. 12. Figure 12a corresponds to Cloud#1 and Figure 12b, to Cloud#2. To evaluate the variability of the turbulent dispersion of the two particle clouds, we have computed the ensemble average of 40 time-evolutions (20 for each cloud) of the squared particle separations for clouds released at different times during a period of 40 non-dimensional time units. The vertical span of the shaded areas in Fig. 12 corresponds to plus/minus one standard deviation of the instantaneous mean values, which are plotted with continuous lines. The red, green and blue lines indicate the evolution of D_{xyz}^{**2}, D_{xy}^{**2} and D_{z}^{**2}, respectively. In Figure 12a, corresponding to Cloud#1, the shaded areas for the different particle separations have been indicated with the same color code (i.e., light red for D_{xyz}^{**2}, light green for D_{xy}^{**2} and light blue for D_{z}^{**2}). On the other hand, for Cloud#2, the time evolutions of D_{xyz}^{**2}, D_{xy}^{**2} and D_{z}^{**2}as well as their standard deviations are very similar and, for clarity, in Figure 12b, the grey shaded area corresponds to the standard deviation of D_{z}^{**2}, which is the largest one.

It can be seen that the time-evolutions of the three mean squared separations of the cloud released in the center of the cavity (Fig. 12b) follow, on average, the same trend and reach their limiting values, corresponding to the perfectly mixed situation ($D_{xyz}^{**2} = D_{xy}^{**2} = D_{z}^{**2} = 1$), at about 80 non-dimensional time units. Considering an average non-dimensional velocity scale of 0.1 for the large-scale circulation (see. Fig. 3). Such a span corresponds to approximately two large-eddy turnover times. In contrast, the time evolutions of the separations of the particles released near one corner of the cavity (Cloud#1, Fig. 12a) behave distinctly. While the mean separation within the plane of the large-scale circulation, D_{xy}^{**2}, reaches the value of a perfectly uniform particle distribution, relatively fast (at about 40 non-dimensional time units), the mean separation of the particles along the z direction increases, for $t^* > 10$, at a lower rate and reaches the limiting value only at $t^* \approx 100$. This indicates a more effective mixing within the plane of the large-scale circulation than along the z direction. Note also that the release of Cloud#2 in the geometric center of the cavity is more effective for dispersing particles along the z direction than the release of Cloud#1 near the bottom of one lateral adiabatic wall, relatively far from the opposite adiabatic lateral wall. Figure 12a shows an overshoot of the time evolution of D_{xy}^{**2} at $t^* \approx 5$. This time corresponds to that required by the fastest transported particles (namely those transported by the large-scale recirculation) to reach the top wall of the cavity and bend towards the horizontal direction (see Fig. 11, Multimedia available online). This change in direction produces a temporary reduction of the mean particle distance observed in the time evolution of D_{xy}^{**2}, and to a lesser extend in the time-evolution of D_{xyz}^{**2}. In contrast the time-evolutions of Cloud#2 (Fig. 12b) show monotonic increases in the mean squared distances. Figure 12a

shows that the largest variability associated with the mean separations is observed for the time-evolutions of D_z^{**2} indicating that within the large-scale circulation the fluctuations along the z direction are more intermittent compared with those in the x or y directions. The variabilities of the distances D_{xyz}^{**2} and D_{xy}^{**2} for Cloud#1 are similar and comparable with those for Cloud#2.

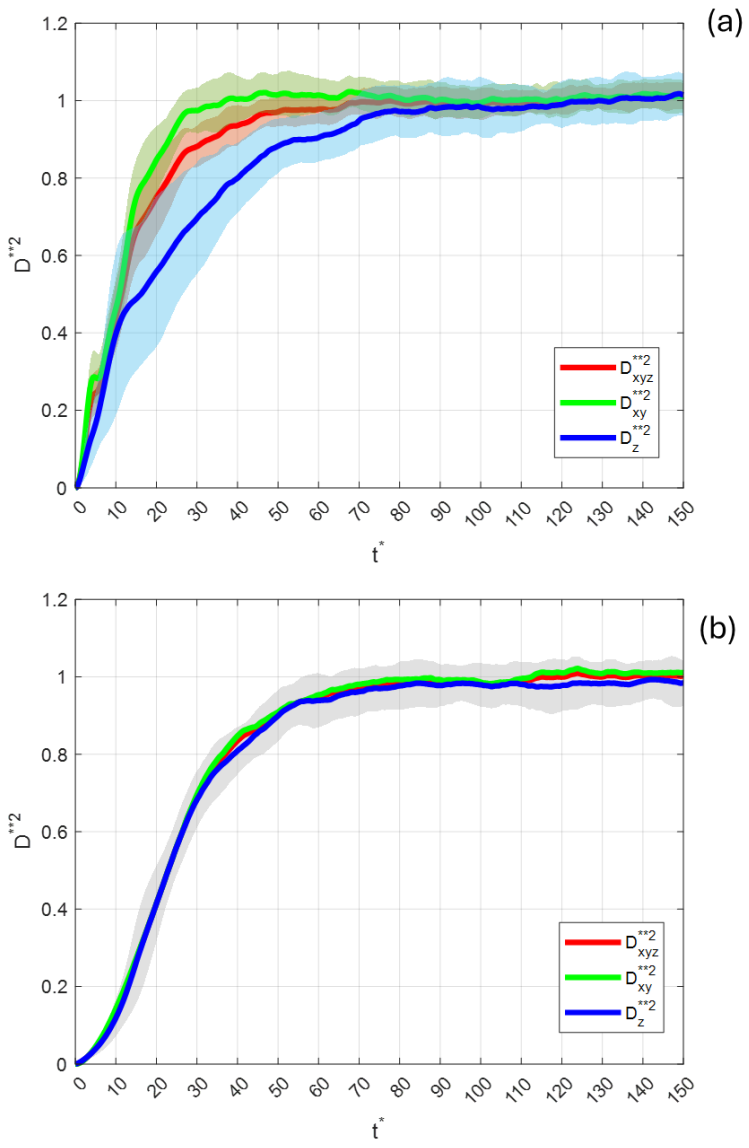

Figure 12. Ensemble average time-evolutions of the non-dimensional mean squared particle separations. (a) Cloud#1. (b) Cloud#2.

The comparisons between the time-evolutions of the mean separations of the different simulations with the mean values predicted by the DNS are plotted in Figures 13 to 17. We grouped the plots according to the simulation technique used: Figure 13 corresponds to LES, Figure 14 to hybrid methods, Figure 15 to SAS, Figure 16 to URANS and Figure 17 to RANS.

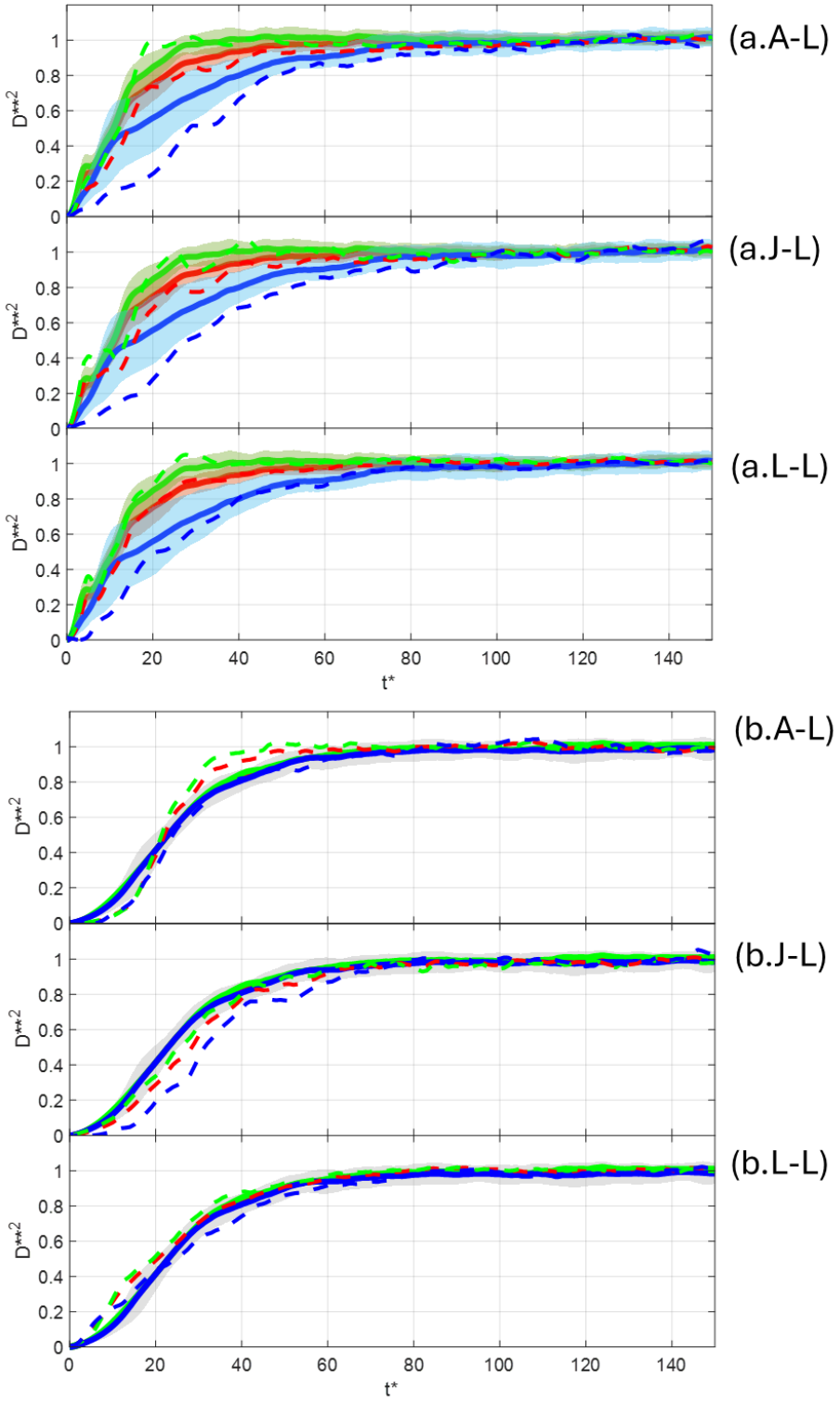

Figure 13. Comparison LES/DNS of the time-evolutions of the non-dimensional mean squared particle separations. Red: D_{xyz}^{**2}. Green: D_{xy}^{**2}. Blue: D_{z}^{**2}. (a) Cloud#1. (b) Cloud#2.

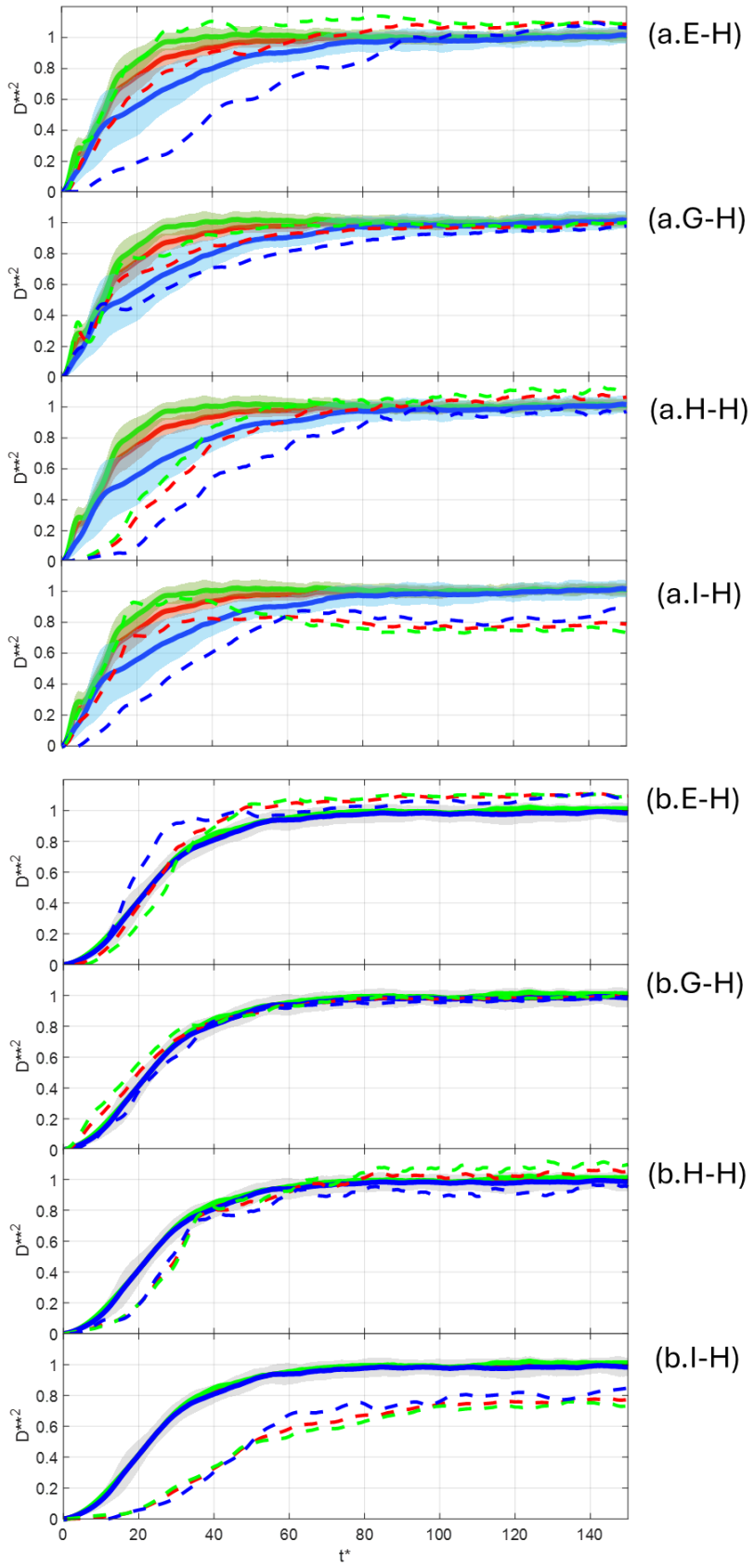

513

514

515 Figure 14. Comparison Hybrid Simulations/DNS of the time-evolutions of the non-dimensional mean

516 squared particle separations. Red: D_{xyz}^{**2}. Green: D_{xy}^{**2}. Blue: D_{z}^{**2}. (a) Cloud#1. (b) Cloud#2.

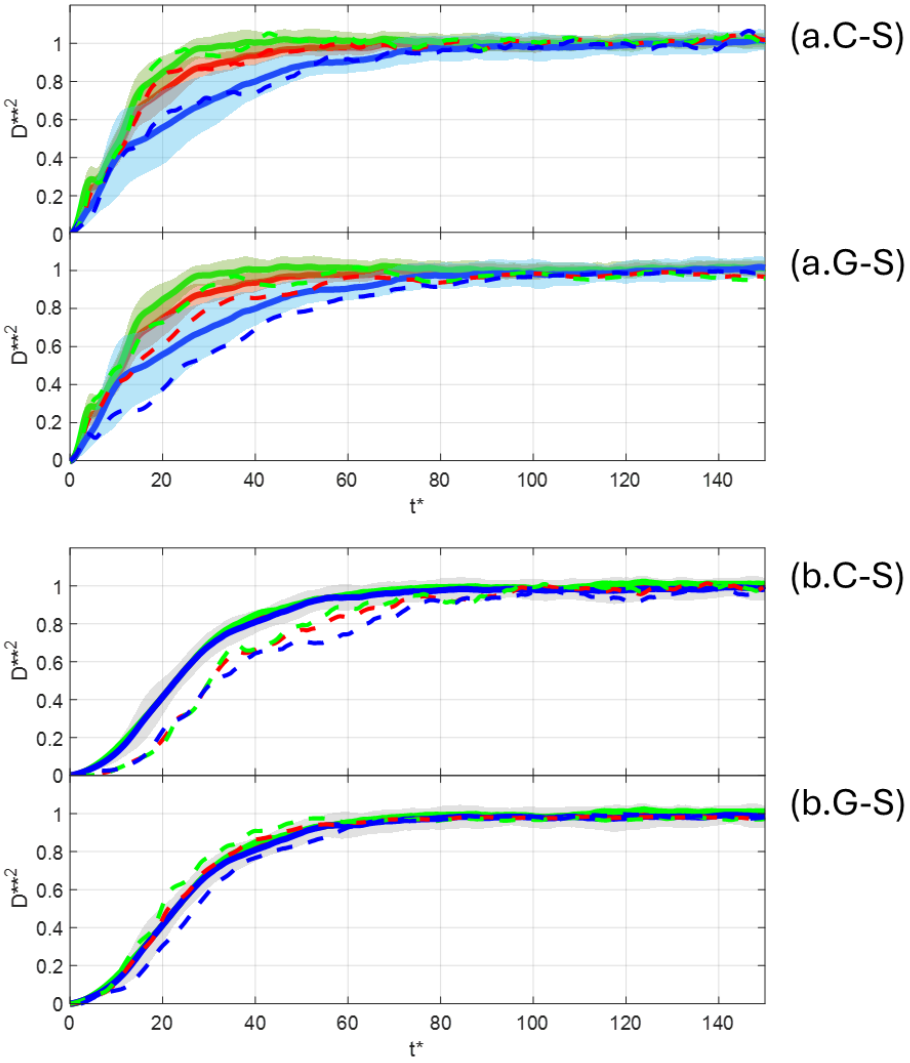

Figure 15. Comparison SAS/DNS of the time-evolutions of the non-dimensional mean squared particle separations. Red: D_{xyz}^{**2}. Green: D_{xy}^{**2}. Blue: D_{z}^{**2}. (a) Cloud#1. (b) Cloud#2.

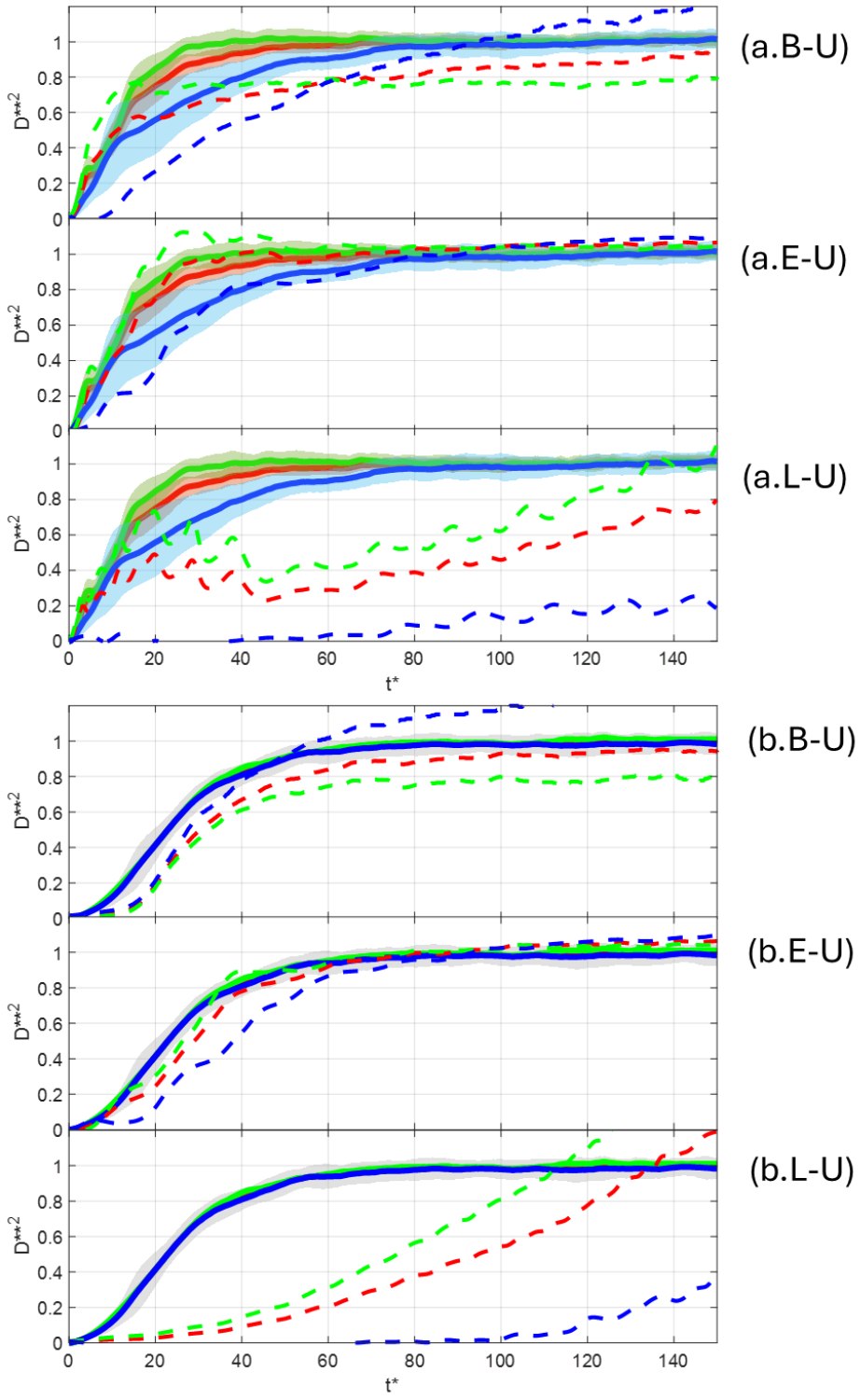

Figure 16. Comparison URANS/DNS of the time-evolutions of the non-dimensional mean squared particle separations. Red: D_{xyz}^{**2}. Green: D_{xy}^{**2}. Blue: D_{z}^{**2}. (a) Cloud#1. (b) Cloud#2.

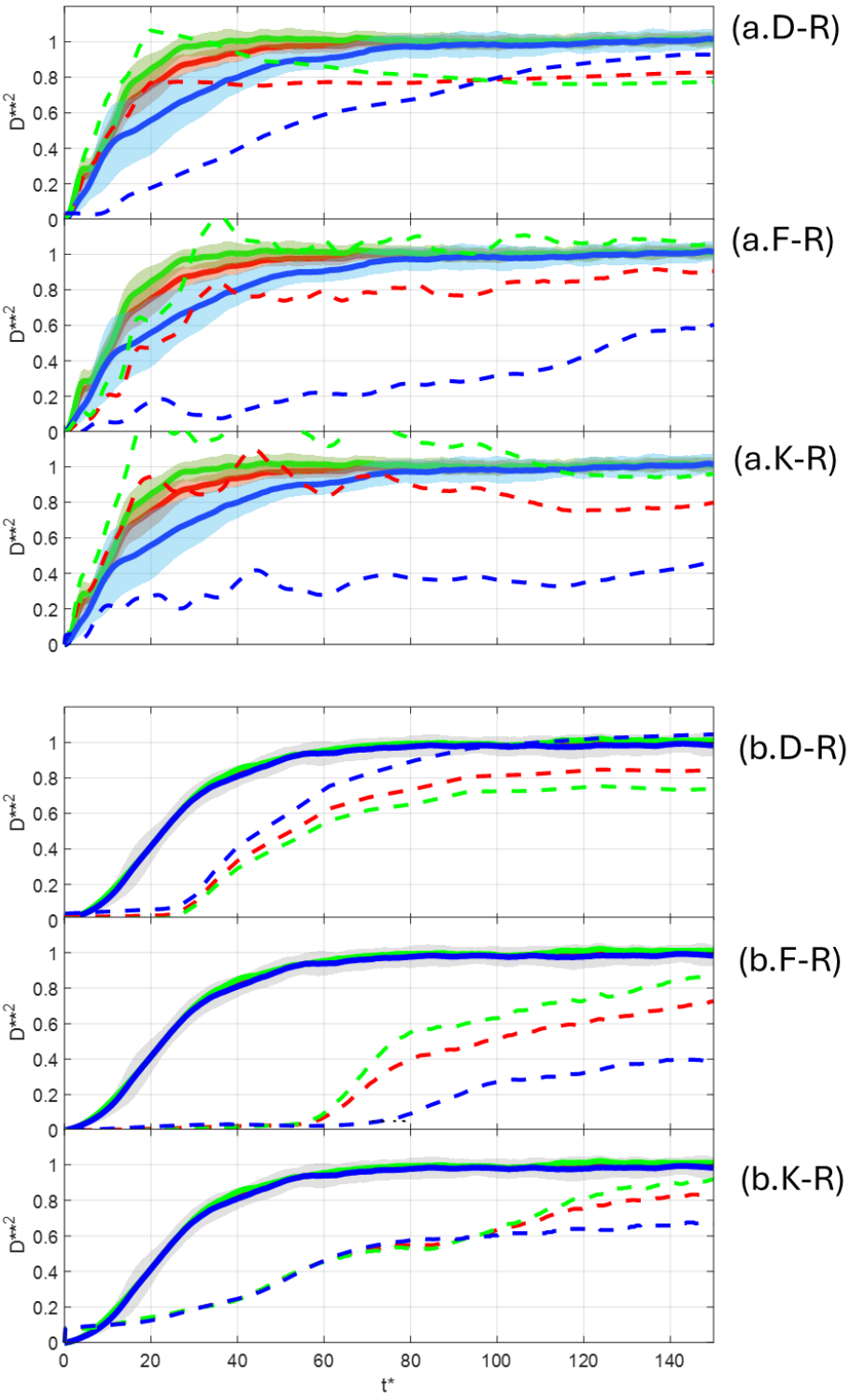

Figure 17. Comparison RANS/DNS of the time-evolutions of the non-dimensional mean squared particle separations. Red: D_{xyz}^{**2}. Green: D_{xy}^{**2}. Blue: D_{z}^{**2}. (a) Cloud#1. (b) Cloud#2.

Figure 13 shows that LES correctly predicts the dispersion of both clouds and that the times at which the mean distances reach the limiting values are comparable with those of DNS (i.e. $D_{xyz}^{**2} = D_{xy}^{**2} = D_{z}^{**2} = 1$ for $t^* \to \infty$). In contrast, the time evolution provided by the hybrid simulations, E-H, H-H

and I-H, plotted in Figure 14, reaches larger (E-H and H-H) or lower (I-H) limiting values in comparison with the theoretical ones, which are equal to unity. This can be attributed to non-uniform final distribution of the particles within the cavity attained at large times for these three simulations. For example, if particles tend to accumulate near the adiabatic walls, then the value of D_z^{*2} at large times will be larger than the theoretical one, ($D_z^{*2}(t \to \infty) = \frac{1}{6}$) and, thus, $D_z^{**2}(t \to \infty)$ will be higher than one (see for example Fig. 14b.E-H). Conversely, if particles tend to accumulate near the centre of the cavity, then $D_z^{*2}(t \to \infty) < 1$ (Fig. 14b.I-H). On the other hand, the simulation G-H predicts correctly the time-evolutions of the different mean separations for the two clouds, as shown in Figures 14a.G-H and 14b.G-H. From the information reported in Table 3, it is difficult to infer the reason behind the better prediction of this hybrid simulation in comparison with simulations E-H, H-H and I-H. However, inspecting the deviations, with respect to DNS, of the time-averaged velocity, temperature and turbulence kinetic profiles shown in Figure 6, reveals that, except for simulation I-H, the hybrid simulations (E-H, G-H, H-H) show similar deviations of the turbulence kinetic energy (Fig. 6b) but the velocity and temperature profiles of simulation G-H agree better with the DNS than those corresponding to simulations E-H, H-H and I-H.

The time evolutions of the particle distances predicted by the two SAS are plotted in Figure 15. Both simulations are within the variability of the dispersion of Cloud#1 provided by the different DNS realizations. For Cloud#2 (Figs. 15b.C-S and 15b.G-S) the dispersion is slightly underpredicted in the case of the simulation C-S while the simulation G-S agrees very well with the DNS. This agreement is also observed for the turbulence kinetic energy distributions shown in Figures 9b, 9c, 10b and 10c.

Figure 16 shows that the URANS simulation E-U reproduces the DNS fairly well, reaching a limiting value of the particle distances that is slightly larger than one. In contrast, simulations B-U and L-U and the three RANS simulations, plotted in Figure 17, show significant deviations with respect to the DNS. In particular these simulations underpredict the rate of dispersion of the particle clouds and this agrees with the low levels of turbulence kinetic energy obtained by the URANS and RANS simulations as shown in Figs. 9 and 10. In fact these figures show that the simulation E-U predicts correctly the turbulence kinetic energy distribution while the other RANS (simulations D-R, F-R and K-R) and URANS (B-U and L-U) systematically underestimate the overall turbulence level of the flow (see for example, Figs. 9d, 9f, 9g, 9h and 9i).

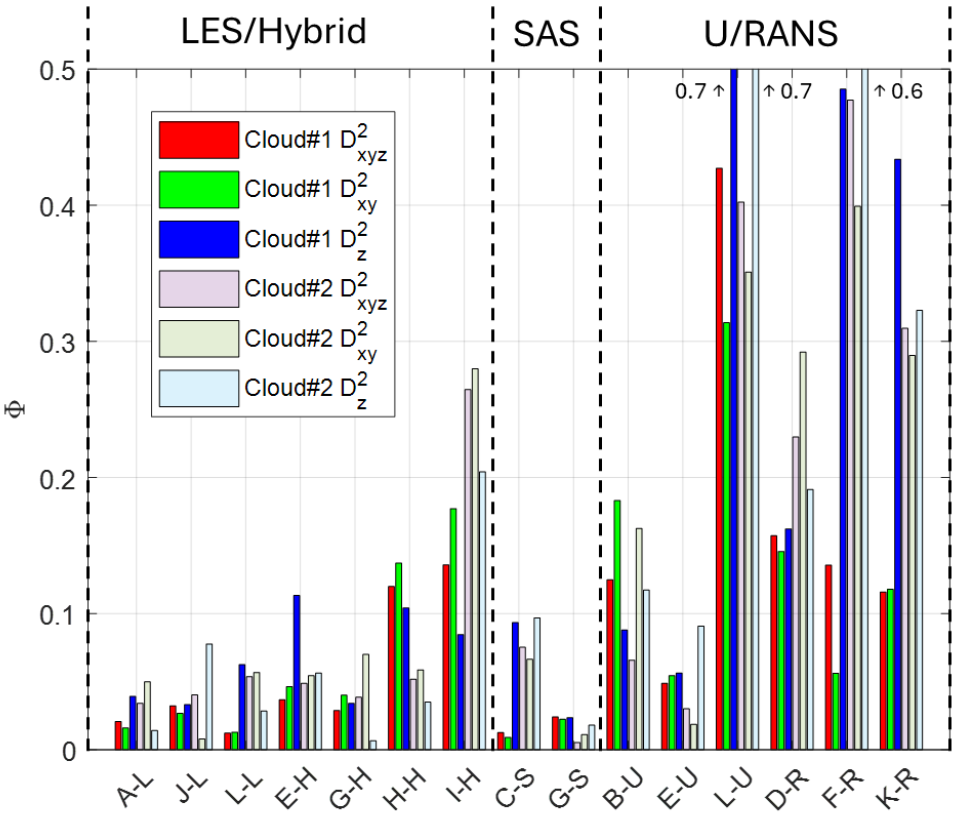

564

565 Figure 18. Differences of the time evolutions of the mean squared particle separations predicted by
566 the different simulations and the DNS.

567

568 Lagrangian particle dispersion in hybrid methods and URANS/RANS flow simulations usually is
569 performed employing stochastic models to incorporate the effect of the instantaneous turbulent
570 fluctuations of the flow in the equations of particle motion (Mofakham and Ahmadi, 2020; Lo et al.,
571 2022). These models, often referred to as Random Walk Models (RWM), extract the fluctuating
572 velocity from the mean flow solution to include the effect of the turbulent flow in the particle path.
573 Commonly, simulations of turbulent flows using URANS and RANS techniques adopt the square root
574 of the turbulence kinetic energy as the velocity scale to compute the fluctuating component of the
575 particle velocity, which has been advected according to the time-averaged velocity field. For the flow
576 conditions considered here, the turbulence kinetic peaks near the wall attaining non-dimensional
577 values roughly equal to 4×10^{-3} (see Fig. 5). This yields a non-dimensional velocity scale for the
578 fluctuations of approximately 0.06. This relatively large value, together with the insensitivity of most
579 of the RWM implemented in commercial and open-source CFD codes to the direction of the
580 fluctuations, can lead to an overestimation of the particle velocity fluctuations towards the wall,
581 artificially increasing particle-wall collisions and the injection of the particles very near the wall, where
582 the particles get trapped due to the low mean velocity and turbulence kinetic energy. This scenario

583 can lead to increased particle concentrations near the walls and produce deviations from the perfectly
584 uniform distribution of particles within the cavity predicted by the DNS at large times ($t^* > 100$) and
585 expected in view of the small Stokes number of the particles ($St = \frac{\rho_p d_p^2 V}{18\mu L} \sim 10^{-8}$).
586
587 To quantify the differences between the averaged values provided by the DNS and the predictions of
588 D_{xyz}^{**2}, D_{xy}^{**2} and D_z^{**2} of the different simulations, we use the deviation parameter, Φ, which was
589 computed as follows. For each time evolution of D_{xyz}^{**2}, D_{xy}^{**2} or D_z^{**2}, we identified the values that lay
590 above the mean value plus one standard deviation of the DNS (reference DNS value, hereinafter). For
591 these values we computed the absolute value of the difference with respect to the reference DNS
592 value. The same procedure was then adopted for the values below the mean value minus one standard
593 deviation of the DNS. Finally, the deviation parameter for the $i\text{-}th$ mean squared separation (i.e., $i \equiv$
594 xyz, xy or z) of the simulation $j\text{-}th$ is defined as the averaged value of such differences.
595
596 $$\Phi = \langle \mathrm{abs}\left[\left(D_i^{**2}(t)\right)^j - \left(D_i^{**2}(t)\right)^{DNS}\right]\rangle \quad (12)$$
597 if
598 $$\left(D_i^{**2}(t)\right)^j > \left(D_i^{**2}(t)\right)^{DNS} + \sigma\left(D_i^{**2}(t)\right)^{DNS} \; or \; \left(D_i^{**2}(t)\right)^j < \left(D_i^{**2}(t)\right)^{DNS} - \sigma\left(D_i^{**2}(t)\right)^{DNS}$$
599
600 where $\sigma\left(D_i^{**2}(t)\right)^{DNS}$ is the standard deviation of the $i\text{-}th$ mean squared separation predicted by the
601 DNS. Figure 18 shows the deviation parameter for the three different mean particle distances of the
602 two clouds and for the different simulations. The LES and hybrid simulations, in general, perform
603 better than the RANS simulations. The exception is the simulation I-H, which shows significant
604 differences, with respect to the DNS of the turbulence kinetic energy (see for example Fig. 8h).
605 Remarkably, the predictions of the SAS, C-S and G-S are also very close to the DNS, and they perform
606 even better, in some cases, than some LES and hybrid simulations. The agreement with the DNS of the
607 dispersion predicted by the URANS simulations depends strongly on the prediction of the turbulence
608 kinetic energy distribution. For example, the simulation E-U with a similar distribution of the
609 turbulence kinetic energy as the DNS (see Fig. 10e) is characterized by a lower deviation parameter
610 than the simulations B-U and L-U. We recall here that the grid resolutions of these three URANS
611 simulations are 0.4 M nodes for B-U and 2 M nodes for E-U and L-U and also that the turbulence
612 models used are $k\text{-}\varepsilon$ for B-U and L-U and $k\text{-}\omega$ for E-U (see Table 3). This suggests that the better
613 performance of the simulation E-U can be attributed to the combination of an adequate grid
614 resolution together with the use of the $k\text{-}\omega$ turbulence model.
615

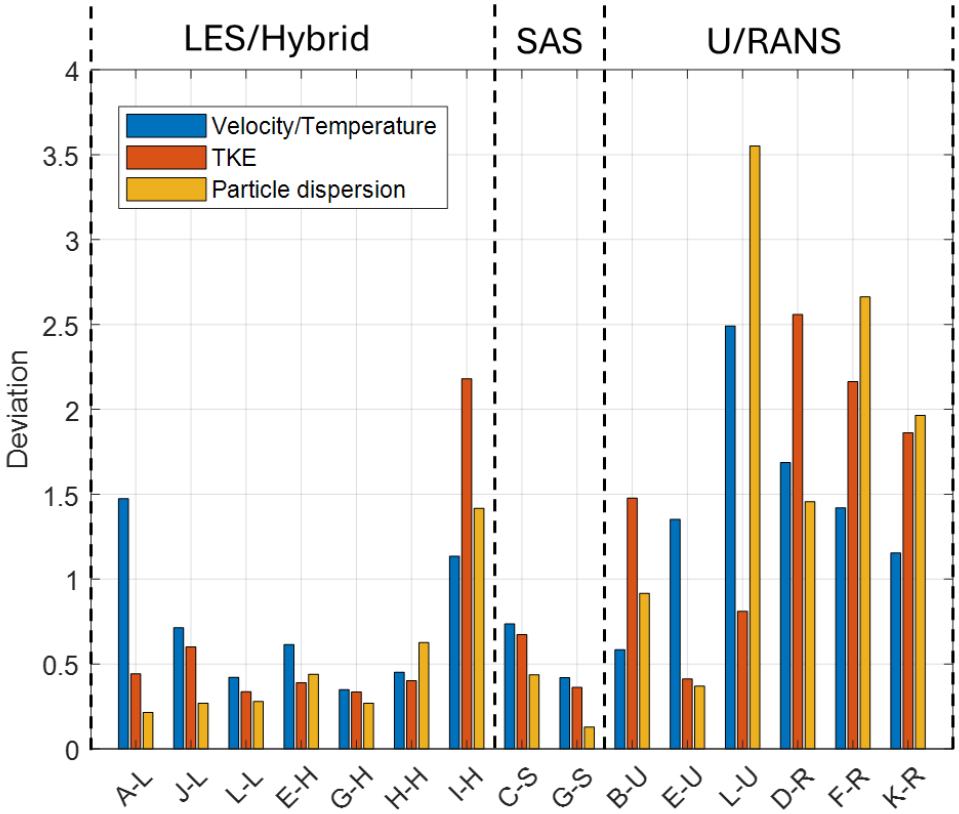

Figure 19. Deviations, with respect to the DNS, of the time-averaged velocity/temperature fields, the turbulent kinetic energy and the particle dispersion.

To summarize the comparison of the different simulations we plotted in Figure 19 the differences, with respect to DNS, of the information shown in two previous figures: Figure 6, corresponding to the deviations of the profiles of velocity, temperature and turbulence kinetic energy and Figure 18, corresponding to the deviations of the particle dispersion. For each simulation we have averaged the four bars of Figure 6a, the two bars of Figure 6b and the six bars of Figure 18, scaling the resulting averaged values with the mean for all the simulations. These scaled deviations are plotted in Figure 19 and are accompanied by three bars. The blue bar indicates jointly the differences in the velocity and temperature profiles, the red bar corresponds to the differences in the turbulence kinetic energy and the orange bar to the difference in the particle dispersion. It can be seen that, in general, significant deviations of the turbulence kinetic energy leads to relatively large deviations of the particle dispersion. The exception is the simulation L-U which shows good agreement with the DNS when comparing the turbulence kinetic energy profiles (Figs. 5b and 5d) but shows substantial differences when considering the spatial distributions of the turbulence kinetic energy (compare for example Figs. 10a and 10f). The differences in the velocity and temperature profiles are not strongly correlated with the differences in the particle dispersion. For example, simulations A-L and E-U show differences in the velocity and temperature profiles but predict reasonably well the cloud dispersion.

4. CONCLUSIONS

In this paper we presented and discussed the outcomes of a benchmark study conducted within the framework of an International CFD Challenge. The study aimed to assess the performance of various numerical and turbulence modelling techniques to simulate the turbulent free convection flow and the dispersion of particles within a room-sized enclosure. Twelve research teams have contributed to the Challenge and individually conducted a total of fifteen simulations of the same flow configuration, for which a reference Direct Numerical Simulation (DNS) is available. The database generated consists of three Large-Eddy Simulations (LES), four hybrid LES/RANS (Reynolds-Averaged Navier-Stokes) simulations, two Scale Adaptive Simulations (SAS), three Unsteady Reynolds-Averaged Navier-Stokes (URANS) simulations and three RANS simulations. Results of the mean flow quantities and metrics of the dispersion of two clouds of particles are compared with each other and with the DNS results.

The mean flow quantities, as the surface averaged Nusselt numbers, time-averaged velocity and temperature profiles and the turbulence kinetic energy are, in general, well reproduced by the LES and the hybrid methods. In the case of different simulations performed with hybrid methods the grid resolution seems to be the cause for significant deviations when the grid is too coarse: In particular, this is observed for simulations performed with less than 2M nodes while simulations carried out with 2M nodes or more show much better agreement with the DNS. The two SAS simulations performed with similar grid resolutions as the hybrid simulations both show relatively small deviations, comparable with those provided by the LES or the hybrid simulations. The comparison of the three URANS cases shows that the one performed with the k-ω turbulence model has a better agreement with DNS than the one carried out with the same grid resolution (2M nodes) but using the k-ε model. The third URANS simulation, carried out with less than a quarter of grid nodes than the other two and using the k-ε model, shows larger deviations from DNS, as expected. The RANS simulations also exhibit significant differences with respect to DNS, independent of the grid resolution and the specific turbulence model (k-ε or k-ω) used.

The accuracy of particle dispersion predictions is primarily influenced by the combination of the turbulence model and grid resolution, as the choice of these factors plays a crucial role in accurately reproducing the turbulence kinetic energy. In fact, LES, hybrid simulations and URANS that properly predict the spatial distribution of the turbulence kinetic energy are found to capture the time evolutions of the mean squared separation of the particles, and, thus, the particle dispersion, in good

agreement with DNS. Contrarily, RANS simulations and coarse-grid hybrid simulations that underpredict the overall turbulence intensity of the flow, underpredict the rate of dispersion of the particle clouds, and fail in capturing, for the flow conditions considered, the ultimate perfectly uniform distribution of the particles within the cavity.

Supplementary Material

The flyer announcing the Challenge and the Instruction document for participation are included as Supplementary Material.

The details of the turbulence models employed in the simulations, as well as information about the models used for the various terms in the particle force balance, are also provided as Supplementary Material.

Acknowledgements

BF and AM acknowledge the use of ARCHER2 UK National Supercomputing Service. (https://www.archer2.ac.uk).

DFF and KI acknowledge the use of the National Computational Infrastructure (NCI) which is supported by the Australian Government, and accessed through the Sydney Informatics Hub HPC Allocation Scheme, which is supported by the Deputy Vice-Chancellor (Research), University of Sydney.

FD and SS acknowledge the access to the HPC resources of Curie/Irene Rome from TGCC under the allocation A0162A06074 made by GENCI.

JN acknowledges funding by the MWK Baden-Württemberg (ref. no. 32-7545.20/4/59 Mittelbauprogramm).

JP, AF, AL and SC acknowledge the financial funding of projects PID2020-113303GB-C21 and PID2023-146648NB-C21, funded by the Spanish Ministerio de Ciencia e Innovación and the Agencia Estatal de Investigación and the support of the Departament de Recerca i Universitats de la Generalitat de Catalunya under project. 2021SGR00732.

Data availability statement

The data that support the findings of this study are available from the corresponding author upon reasonable request.

Author declarations

The authors have no conflicts to disclose.

713

714 **REFERENCES**

715

716 Ai, Z. T., & Melikov, A. K. (2018). Airborne spread of expiratory droplet nuclei between the occupants
717 of indoor environments: A review. Indoor air, 28(4), 500-524.

718

719 Ansys Fluent (2024) https://www.ansys.com/products/fluids/ansys-fluent

720

721 Bournet, P. E., & Boulard, T. (2010). Effect of ventilator configuration on the distributed climate of
722 greenhouses: A review of experimental and CFD studies. Computers and Electronics in Agriculture,
723 74(2), 195-217.

724

725 Bourouiba, L. (2021). Fluid dynamics of respiratory infectious diseases. Annual Review of Biomedical
726 Engineering, 23(1), 547-577.

727

728 Caciolo, M., Stabat, P., & Marchio, D. (2012). Numerical simulation of single-sided ventilation using
729 RANS and LES and comparison with full-scale experiments. Building and Environment, 50, 202-213.

730

731 Choi, H., Kim, H., & Kim, T. (2019). Long-term simulation for predicting indoor air pollutant
732 concentration considering pollutant distribution based on concept of CRPS index. In Building
733 Simulation (Vol. 12, pp. 1131-1140). Tsinghua University Press.

734

735 Concilio, C., Benito, P. A., Ramírez, C. P., & Viccione, G. (2024). CFD simulation study and
736 experimental analysis of indoor air stratification in an unventilated classroom: a case study in Spain.
737 Heliyon, e32721.

738

739 Cuce, E., Sher, F., Sadiq, H., Cuce, P. M., Guclu, T., & Besir, A. B. (2019). Sustainable ventilation
740 strategies in buildings: CFD research. Sustainable Energy Technologies and Assessments, 36, 100540.

741

742 Dehbi, A., Kalilainen, J., Lind, T., & Auvinen, A. (2017). A large eddy simulation of turbulent particle-
743 laden flow inside a cubical differentially heated cavity. Journal of Aerosol Science, 103, 67-82.

744

745 Delort-Laval, M., Soucasse, L., Rivière, P., & Soufiani, A. (2022). Rayleigh–Bénard convection in a
746 cubic cell under the effects of gas radiation up to Ra = 10^9. International Journal of Heat and Mass
747 Transfer, 187, 122453.
748
749 Demou, A. D., & Grigoriadis, D. G. (2019). Direct numerical simulations of Rayleigh–Bénard
750 convection in water with non-Oberbeck–Boussinesq effects. Journal of Fluid Mechanics, 881, 1073-
751 1096.
752
753 Duchaine F., Cizeron C.N., Odier N., Dombard J., Marchall S., Francois, N., Poinsot, T. (2021) High-
754 performance CFD for Respiratory Droplet Turbulent Dispersion in a Ventilated City Bus, International
755 Journal of Computational Fluid Dynamics, **35**(9), 758-777.
756
757 Fabregat, A. and Pallares, J. (2020). Heat transfer and boundary layer analyses of laminar and
758 turbulent natural convection in a cubical cavity with differently heated opposed walls. International
759 Journal of Heat and Mass Transfer, **151**, 119409.
760
761 Fraga B., Stoesser T., Lai C.C., Socolofsky, S.A. (2016) A LES-based Eulerian–Lagrangian approach to
762 predict the dynamics of bubble plumes, Ocean Modelling, **97**, 27-36.
763
764 Gilani, S., Montazeri, H., & Blocken, B. (2016). CFD simulation of stratified indoor environment in
765 displacement ventilation: Validation and sensitivity analysis. Building and Environment, 95, 299-313.
766
767 Hanjalić, K., & Vasić, S. (1993). Computation of turbulent natural convection in rectangular
768 enclosures with an algebraic flux model. International Journal of Heat and Mass Transfer, 36(14),
769 3603-3624.
770
771 Jones, A. P. (1999). Indoor air quality and health. Atmospheric Environment, 33(28), 4535-4564.
772
773 Kalilainen, J., Rantanen, P., Lind, T., Auvinen, A., & Dehbi, A. (2016). Experimental investigation of a
774 turbulent particle-laden flow inside a cubical differentially heated cavity. Journal of Aerosol Science,
775 100, 73-87.
776

Lavrinenko A., Fabregat A., Gisbert F., Pallares J. (2024) Direct Numerical Simulation of pathogen-laden aerosol dispersion in buoyancy-driven turbulent flow within confined spaces, International Communications in Heat and Mass Transfer, **152**, 107272.

Lavrinenko, A., Gisbert, F., Pallares, J., & Fabregat, A. (2023). Fully-resolved numerical simulations of the turbulent flow and particle deposition in a cubical cavity with two pairs of differentially heated opposed walls at Rayleigh number 3.6×10^9. International Communications in Heat and Mass Transfer, **141**, 106564.

Li, Y., & Nielsen, P. V. (2011). CFD and ventilation research. Indoor Air, 21(6), 442-453.

Li, Z., Wen, Q., & Zhang, R. (2017). Sources, health effects and control strategies of indoor fine particulate matter (PM2. 5): A review. Science of the Total Environment, 586, 610-622.

Lo, C., Bons, J., Yao, Y., & Capecelatro, J. (2022). Assessment of stochastic models for predicting particle transport and deposition in turbulent pipe flows. Journal of Aerosol Science, 162, 105954.

Maity, P., Koltai, P., & Schumacher, J. (2022). Large-scale flow in a cubic Rayleigh–Bénard cell: long-term turbulence statistics and Markovianity of macrostate transitions. Philosophical Transactions of the Royal Society A, 380(2225), 20210042.

Maroni, M., Seifert, B., & Lindvall, T. (Eds.). (1995). Indoor air quality: a comprehensive reference book. Elsevier.

Mofakham, A. A., & Ahmadi, G. (2020). On random walk models for simulation of particle-laden turbulent flows. International Journal of Multiphase Flow, 122, 103157.

Monka, A., Fraga, B., Soper, D. and Hemida, H. (2023) Influence of thermal stratification on the transport of polydispersed expiratory particles. Physics of Fluids, **35**(10), 103304.

Paraview (2024) https://www.paraview.org/

809 Riley, W. J., McKone, T. E., Lai, A. C., & Nazaroff, W. W. (2002). Indoor particulate matter of outdoor
810 origin: importance of size-dependent removal mechanisms. Environmental Science & Technology,
811 36(2), 200-207.
812
813 Salat, J., Xin, S., Joubert, P., Sergent, A., Penot, F., & Le Quere, P. (2004). Experimental and numerical
814 investigation of turbulent natural convection in a large air-filled cavity. International Journal of Heat
815 and Fluid Flow, 25(5), 824-832.
816
817 Scheel, J. D., & Schumacher, J. (2014). Local boundary layer scales in turbulent Rayleigh–Bénard
818 convection. Journal of Fluid Mechanics, 758, 344-373.
819
820 Scheel, J. D., Emran, M. S., & Schumacher, J. (2013). Resolving the fine-scale structure in turbulent
821 Rayleigh–Bénard convection. New Journal of Physics, 15(11), 113063.
822
823 Schønfeld T., Rudgyard M. (1999) Steady and Unsteady Flow Simulations Using the Hybrid Flow
824 Solver AVBP, AIAA Journal **37** (11), 1378–1385.
825
826 Seguel J.M., Merrill R., Seguel D., Campagna A.C. (2017) Indoor Air Quality, American Journal of
827 Lifestyle Medicine 11(4), 284-295.
828
829 Sheikhnejad, Y., Aghamolaei, R., Fallahpour, M., Motamedi, H., Moshfeghi, M., Mirzaei, P. A., &
830 Bordbar, H. (2022). Airborne and aerosol pathogen transmission modeling of respiratory events in
831 buildings: An overview of computational fluid dynamics. Sustainable Cities and Society, 79, 103704.
832
833 Shen, C., Gao, N., & Wang, T. (2013). CFD study on the transmission of indoor pollutants under
834 personalized ventilation. Building and Environment, 63, 69-78.
835
836 Shim, G., Narayanan, S. R., & Yang, S. (2023). Numerical simulation of virus-laden aerosol
837 transmission in real human respiratory airways. Physics of Fluids, 35(10).
838
839 Soucasse, L., Podvin, B., Rivière, P., & Soufiani, A. (2019). Proper orthogonal decomposition analysis
840 and modelling of large-scale flow reorientations in a cubic Rayleigh–Bénard cell. Journal of Fluid
841 Mechanics, 881, 23-50.
842

STAR-CCM+ (2024) https://www.plm.automation.siemens.com/global/en/products/simcenter/STAR-CCM.html

Tan, Z., & Zhang, Y. (2003). An overview of particulate matter in indoor environments: sources and effects. ASHRAE Transactions, 109, 89-100.

Teimurazov, A., Reiter, P., Shishkina, O., & Frick, P. (2021). Heat transport in a cell heated at the bottom and the side. Europhysics Letters, 134(3), 34001.

Tric, E., Labrosse, G., & Betrouni, M. (2000). A first incursion into the 3D structure of natural convection of air in a differentially heated cubic cavity, from accurate numerical solutions. International Journal of Heat and Mass Transfer, 43(21), 4043-4056.

van Hooff, T., Blocken, B., & Tominaga, Y. (2017). On the accuracy of CFD simulations of cross-ventilation flows for a generic isolated building: Comparison of RANS, LES and experiments. Building and Environment, 114, 148-165.

Vasiliev, A., Frick, P., Kumar, A., Stepanov, R., Sukhanovskii, A., & Verma, M. K. (2019). Transient flows and reorientations of large-scale convection in a cubic cell. International Communications in Heat and Mass Transfer, 108, 104319.

Velasco L. J., Venturi D. N., Fontes D. H., de Souza F. J. (2022) Numerical simulation of drag reduction by microbubbles in a vertical channel, European Journal of Mechanics - B/Fluids, **92**, 215-225.

Villafruela, J. M., Olmedo, I., De Adana, M. R., Méndez, C., & Nielsen, P. V. (2013). CFD analysis of the human exhalation flow using different boundary conditions and ventilation strategies. Building and Environment, 62, 191-200.

Wang, P., Zhang, Y., & Guo, Z. (2017). Numerical study of three-dimensional natural convection in a cubical cavity at high Rayleigh numbers. International Journal of Heat and Mass Transfer, 113, 217-228.

Weller, H., Tabor, G., Jasak, H., & Fureby, C. (1998). A tensorial approach to computational continuum mechanics using object-oriented techniques. Computers in Physics, 12, 620.

World Health Organization. Regional Office for Europe. (2010). WHO guidelines for indoor air quality: selected pollutants. World Health Organization. Regional Office for Europe.

Xu, G., & Wang, J. (2017). CFD modeling of particle dispersion and deposition coupled with particle dynamical models in a ventilated room. Atmospheric Environment, 166, 300-314.

Yang, R., Ng, C. S., Chong, K. L., Verzicco, R., & Lohse, D. (2022). Do increased flow rates in displacement ventilation always lead to better results? Journal of Fluid Mechanics, 932, A3.

Yerragolam, G. S., Howland, C. J., Yang, R., Stevens, R. J., Verzicco, R., & Lohse, D. (2024). Effect of airflow rate on CO2 concentration in downflow indoor ventilation. Indoor Environments, 1(2), 100012.

Figure captions

Figure 1. Sketch of the cubical cavity and the coordinates. Hot/Cold walls are indicated in red/blue. The arrows show the rotation of the large-scale flow circulation.

Figure 2. Differences in the surface-averaged Nusselt numbers on the horizontal (Nu_h) and vertical (Nu_v) walls.

Figure 3. Non-dimensional time-averaged velocity profiles along the horizonal (a and b) and vertical (c and d) bisectors of the vertical symmetry plane of the cavity ($z = 0$).

Figure 4. Non-dimensional time-averaged temperature profiles along the horizonal (a and b) and vertical (c and d) bisectors of the vertical symmetry plane of the cavity ($z = 0$).

Figure 5. Non-dimensional turbulence kinetic energy profiles along the horizonal (a and b) and vertical (c and d) bisectors of the vertical symmetry plane of the cavity ($z = 0$).

Figure 6. Root mean squared differences, between the different predictions and the DNS, in the profiles of (a) velocity and temperature and (b) turbulence kinetic energy along the horizonal and vertical bisectors of the vertical symmetry plane of the cavity ($z = 0$). The values of the bars above the maximum scale of the vertical axis are indicated.

Figure 7. Contours of the turbulence kinetic energy on the vertical symmetry plane of the cavity ($z = 0$).

Figure 8. Contours of the turbulence kinetic energy on the horizontal mid plane of the cavity ($y = 0$).

Figure 9. Contours of the turbulence kinetic energy on the vertical symmetry plane of the cavity ($z = 0$).

Figure 10. Contours of the turbulence kinetic energy on the horizontal mid plane of the cavity ($y = 0$).

925 Figure 11. Time evolution of the dispersion of the particles. (a) Cloud#1. (b) Cloud#2. (a-1) and (b-1)
926 correspond to $t^* = 0$ and (a-2) and (b-2) to $t^* = 5$. (Multimedia available online).
927
928 Figure 12. Ensemble average time-evolutions of the non-dimensional mean squared particle
929 separations. (a) Cloud#1. (b) Cloud#2.
930
931 Figure 13. Comparison LES/DNS of the time-evolutions of the non-dimensional mean squared
932 particle separations. Red: D_{xyz}^{**2}. Green: D_{xy}^{**2}. Blue: D_z^{**2}. (a) Cloud#1. (b) Cloud#2.
933
934 Figure 14. Comparison Hybrid Simulations/DNS of the time-evolutions of the non-dimensional mean
935 squared particle separations. Red: D_{xyz}^{**2}. Green: D_{xy}^{**2}. Blue: D_z^{**2}. (a) Cloud#1. (b) Cloud#2.
936
937 Figure 15. Comparison SAS/DNS of the time-evolutions of the non-dimensional mean squared
938 particle separations. Red: D_{xyz}^{**2}. Green: D_{xy}^{**2}. Blue: D_z^{**2}. (a) Cloud#1. (b) Cloud#2.
939
940 Figure 16. Comparison URANS/DNS of the time-evolutions of the non-dimensional mean squared
941 particle separations. Red: D_{xyz}^{**2}. Green: D_{xy}^{**2}. Blue: D_z^{**2}. (a) Cloud#1. (b) Cloud#2.
942
943 Figure 17. Comparison RANS/DNS of the time-evolutions of the non-dimensional mean squared
944 particle separations. Red: D_{xyz}^{**2}. Green: D_{xy}^{**2}. Blue: D_z^{**2}. (a) Cloud#1. (b) Cloud#2.
945
946 Figure 18. Differences of the time evolutions of the mean squared particle separations predicted by
947 the different simulations and the DNS.
948
949 Figure 19. Deviations, with respect to the DNS, of the time-averaged velocity/temperature fields, the
950 turbulent kinetic energy and the particle dispersion.
951